How does vertical wind shear influence updraft characteristics and hydrometeor distributions in supercell thunderstorms?

Jake P. Mulholland,[a] Christopher J. Nowotarski,[b] John M. Peters,[c] Hugh Morrison,[d] and Erik R. Nielsen[b]

[a] *University of North Dakota, Grand Forks, ND*

[b] *Texas A&M University, College Station, TX*

[c] *Pennsylvania State University, State College, PA*

[d] *National Center for Atmospheric Research, Boulder, CO*

Corresponding author: Jake P. Mulholland, jake.mulholland@und.edu

File generated with AMS Word template 2.0

Early Online Release: This preliminary version has been accepted for publication in *Monthly Weather Review*, may be fully cited, and has been assigned DOI 10.1175/MWR-D-23-0166.1. The final typeset copyedited article will replace the EOR at the above DOI when it is published.

ABSTRACT

Vertical wind shear is known to affect supercell thunderstorms by displacing updraft hydrometeor mass downshear, thereby facilitating the storms' longevity. Shear also impacts the size of supercell updrafts, with stronger shear leading to wider, less dilute, and stronger updrafts with likely greater hydrometeor production. To more clearly define the role of shear across different vertical layers on hydrometeor concentrations and displacements relative to supercell updrafts, a suite of idealized numerical model simulations of supercells was conducted. Shear magnitudes were systematically varied across the 0–1 km, 1–6 km, and 6–12 km AGL layers while the thermodynamic environment was held fixed. Simulations show that as shear magnitude increases, especially from 1–6 km, updrafts become wider and less dilute with an increase in hydrometeor loading, along with an increase in the low-level precipitation area/rate and total precipitation accumulation. Even with greater updraft hydrometeor loading amid stronger shear, updrafts are more intense in stronger shear simulations due to larger thermal buoyancy owing to wider, less dilute updraft cores. Furthermore, downshear hydrometeor displacements are larger in environments with stronger 1–6 km shear. In contrast, there is relatively less sensitivity of hydrometeor concentrations and displacements to variations in either 0–1 km or 6–12 km shear. Results are consistent across free tropospheric relative humidity sensitivity simulations, which show an increase in updraft size and hydrometeor mass with increasing free tropospheric relative humidity owing to a reduction in entrainment-driven dilution for wider updrafts in moister environments.

SIGNIFICANCE STATEMENT

Rotating thunderstorms, known as supercells, are able to persist for multiple hours. One common explanation is that large changes in wind speed and/or direction with height, or shear, transport rain/hail away from supercell updrafts, supporting their maintenance. The strong shear within supercell environments, however, may also lead to greater rail/hail amounts, thereby leading to weaker storms due to this extra mass of water/ice within updrafts. Furthermore, the impact of shear across different height layers on supercell rain/hail characteristics has not been thoroughly investigated. In this study, computer simulations of supercells were conducted to determine that shear occurring between 1–6 km above ground level has a large impact on rain/hail distribution in supercells, and that stronger shear in this layer leads to wider/stronger supercells with greater rain/hail accumulations at the surface.

Accepted for publication in *Monthly Weather Review*. DOI 10.1175/MWR-D-23-0166.1.

Additionally, some of the extra mass of water/ice is transported farther away from updrafts due to the stronger environmental storm-relative winds.

1. Introduction

Vertical wind shear (hereafter "shear") has long been known to increase supercell thunderstorm updraft strength and longevity by increasing the horizontal separation between the main updraft (and mesocyclone), downdrafts, and precipitation (e.g., Brooks et al. 1994a,b; Markowski and Richardson 2010). Studies have shown a strong positive correlation between shear strength and deep convective updraft area, including for supercells (Dennis and Kumjian 2017; Trapp et al. 2017; Warren et al. 2017, Marion and Trapp 2019; Peters et al. 2019; Mulholland et al. 2020; Peters et al. 2020b). In environments with stronger shear, and thus stronger low-level storm-relative inflow in the layer with non-zero CAPE and zero/limited CIN (i.e., the "effective inflow layer", or EIL; Thompson et al. 2007), supercell updrafts grow wider and are less susceptible to entrainment-driven dilution of buoyancy, leading to stronger upward vertical velocities (e.g., Peters et al. 2020b). Supercells amid stronger shear also exhibit stronger non-linear dynamic perturbation pressure gradient accelerations owing to more rapidly rotating updrafts, leading to stronger low-to-mid-level updrafts (e.g., Weisman and Klemp 1984; McCaul and Weisman 1996; Weisman and Rotunno 2000; Peters et al. 2019). While connections between shear, supercell updraft area, and vertical velocities have been firmly established, an extension of these effects on the amount and spatial extent of condensate and precipitation produced by supercells has received comparatively less attention. Do wider, less dilute, and stronger updrafts in stronger shear environments support more hydrometeor mass, leading to greater hydrometeor loading within updrafts? Or does this extra hydrometeor mass get transported downshear of updrafts owing to the stronger storm-relative winds associated with stronger shear? It is also not known which shear layer (i.e., height range over which shear is distributed) has the most relative impact on condensate and precipitation production and location within supercells, and if these impacts depend on environmental free tropospheric relative humidity.

The amount of condensate/hydrometeor mass formed within updrafts is important to help determine: (1) how much buoyancy updrafts actually realize owing to the negative effects of hydrometeor loading on updraft buoyancy (e.g., Emanuel 1994) and (2) any updraft buoyancy "enhancement" if additional (unfrozen) condensate is lofted upward past the freezing level and then freezes, leading to additional latent heating (e.g., Rosenfeld et al. 2008). Furthermore,

Accepted for publication in *Monthly Weather Review*. DOI 10.1175/MWR-D-23-0166.1.

knowledge of the location, spatial extent, and intensity of precipitation from supercells is vital as this has direct hydrological implications, such as flash flooding potential, along with dictating where evaporatively driven downdrafts and cold pools typically develop. Downdrafts and their attendant cold pools have long been hypothesized to be important for supercell tornadogenesis by re-orienting near-surface horizontal vorticity into the vertical direction (e.g., Davies-Jones 1982; Davies-Jones and Brooks 1993) and cold pools foster zones of enhanced horizontal baroclinic vorticity along with regions of enhanced horizontal vorticity stretching (e.g., the "streamwise vorticity current"; Orf et al. 2017; Schueth et al. 2021; Finley et al. 2023), which may be vital to low-level mesocyclone formation/intensification along with tornado potential/maintenance (e.g., Klemp and Rotunno 1983; Rotunno and Klemp 1985; Wicker and Wilhelmson 1995; Adlerman et al. 1999; Markowski et al. 2012; Beck and Weiss 2013; Tanamachi et al. 2013; Markowski and Richardson 2014; Orf et al. 2017; Schueth et al. 2021; Finley et al. 2023). Furthermore, the rear-flank downdraft has been shown to be important for low-level mesocyclone (e.g., "vortex arches"; Straka et al. 2007) and tornado formation (e.g., "internal surges"; Lee et al. 2012; Skinner et al. 2014; Schenkman et al. 2016). Gray and Frame (2021) showed that varying the 3–6 km AGL shear vector orientation shifted the location of low-level hydrometeor loading and downdrafts, and subsequently, the location of low-level baroclinic zones within simulated supercells (see their Fig. 11). Parker (2017) also showed that altering the mid-to-upper-level (i.e., > 4 km) hodograph orientation shifted the location of near-surface precipitation within simulated supercells (see their Fig. 3). Furthermore, the location and strength of downdrafts and cold pools in supercells may impact whether supercell updrafts are subsequently undercut by surging outflows (Brooks et al. 1994b; Finley et al. 2001; Mashiko et al. 2009; Schenkman et al. 2016). Lastly, condensate that is lofted and advected downshear of supercell updrafts may alter inflow air properties (e.g., CAPE, shear, vorticity, etc.) through effects such as anvil shading and a corresponding reduction in surface heat fluxes and boundary layer mixing (Frame and Markowski 2010, 2013; Nowotarski and Markowski 2016).

The few studies that have, at least tangentially, investigated the impact of shear on supercell updraft area and condensate/precipitation characteristics are briefly summarized here. Observational studies have utilized dual-polarization Doppler weather radar to: (1) quantify hydrometeor size sorting (e.g., differential reflectivity "arcs"; specific differential phase "footprints") patterns owing to differences in low-level storm-relative winds (e.g., Loeffler and Kumjian 2018; Loeffler et al. 2020); and (2) infer updraft size characteristics (e.g., differential

Accepted for publication in *Monthly Weather Review*. DOI 10.1175/MWR-D-23-0166.1.

reflectivity “columns”; e.g., French and Kingfield 2021) in supercells. In terms of numerical model simulation studies, Dennis and Kumjian (2017) showed that simulated supercells amid environments with stronger 3–6 km shear exhibited wider updrafts and consequently a wider region of hail mass. Warren et al. (2017) showed that simulated supercells in environments with stronger upper-level (6–12 km) shear produced a larger areal extent of precipitation in additional to greater precipitation accumulations, which differed from the observed sounding-based results of Rasmussen and Straka (1998). Specifically, Rasmussen and Straka (1998) found that low-precipitation supercells were associated with stronger upper-level storm-relative winds. A conference presentation by Frame and Nelson (2022) analyzed low-precipitation versus high-precipitation supercell environments and found results more consistent with those depicted in Warren et al. (2017) in that stronger shear was more often associated with the high-precipitation supercell mode. Supercells in the stronger upper-level shear simulations of Warren et al. (2017) exhibited stronger low-level storm-relative inflow. This stronger low-level storm-relative inflow resulted in wider updrafts with greater upward vertical mass flux and condensate production. Peters et al. (2019) and Mulholland et al. (2020) also showed an increase in the areal extent and surface accumulation of precipitation within simulated supercells amid stronger environmental shear owing to the physical processes outlined in Warren et al. (2017) and explained by the theoretical framework presented in Peters et al. (2019). Furthermore, moderate to strong linear correlation coefficients (> 0.5) between shear magnitude and the spatial extent of updraft and rain water aloft for simulated supercells were noted in Snyder et al. (2017).

Trapp et al. (2017) and Marion and Trapp (2019) suggested a direct connection between updraft area, downdraft area, and precipitation area in simulated supercells. These two studies argue that the horizontal scale of the updraft should correspond to the horizontal scale of the downdraft owing to the downdraft size being strongly influenced by the spatial extent of evaporating rain and melting graupel/hail formed in the updraft. Marion and Trapp (2019) specifically showed a robust positive relationship between time-averaged updraft area and precipitation area at 7 km with a coefficient of determination (r^2) of 0.70 (see their Fig. 17), but these authors did not analyze surface precipitation area. Jo and Lasher-Trapp (2022, 2023) found that supercell updrafts within stronger shear environments were wider and less dilute, therefore resulting in greater condensate production, but because some of this additional condensate was detrained from the cloud, transported downshear, and evaporated or sublimated, overall precipitation efficiency was relatively low (generally < 40%). Nielsen and

Accepted for publication in *Monthly Weather Review*. DOI 10.1175/MWR-D-23-0166.1.

Schumacher (2018) found that by increasing low-level shear in idealized numerical model simulations, supercell updrafts exhibited stronger low-level rotation, and thus were able to dynamically ingest near-surface stable air with higher moisture content, thereby resulting in higher precipitation rates than weaker low-level shear simulations. Nielsen and Schumacher (2020) further showed, via a case study of a heavy rainfall event using the Weather Research and Forecasting model, that increased low-level rotation owing to ambient strong low-level shear led to a more efficient warm rain process, and thus, heavier rainfall rates/accumulations.

The aforementioned studies generally did not specifically focus on the impact of shear on hydrometeor distribution in supercells. It is not known how variations in shear magnitude across specific layers (e.g., lower, middle, or upper troposphere) influence the amount and location of hydrometeor mass within supercells. In addition to potential shear impacts, previous studies reached differing conclusions related to the effects of relative humidity (RH) on hydrometeor and precipitation distribution in supercells. For example, Gilmore and Wicker (1998) used idealized numerical model simulations of supercells to demonstrate that lower low-to-mid-tropospheric RH led to stronger downdrafts and cold pools via enhanced evaporative cooling, with an increasing propensity for surging outflows to undercut supercell updrafts. In contrast, James and Markowski (2010) found that lower low-to-mid-tropospheric RH reduced upward vertical mass flux, condensation rates, and precipitation accumulations owing to enhanced evaporation of rain and sublimation of ice in the drier ambient environment surrounding clouds in idealized supercell simulations. James and Markowski (2010) proposed that the use of a warm-rain-only microphysics parameterization scheme in the Gilmore and Wicker (1998) simulations may have resulted in these contrasting results. Grant and van den Heever (2014) used simulations with varying low-to-mid-tropospheric RH to show that supercells forming in environments with reduced RH had greater evaporation rates, sharper cloud edges, and narrower updrafts, and thus, were more toward the low-precipitation end of the supercell spectrum with smaller precipitation areas near the surface. Jo and Lasher-Trapp (2023) used idealized numerical model simulations of supercells with varying mid-to-upper tropospheric RH and found similar results to James and Markowski (2010), owing to increased anvil-level downshear detrainment amid stronger shear (Jo and Lasher-Trapp 2022).

Based on the gaps in understanding outlined above, we specifically address the follow research questions:

Accepted for publication in *Monthly Weather Review*. DOI 10.1175/MWR-D-23-0166.1.

1) *How does systematically varying shear magnitude across different vertical layers affect hydrometer concentration and displacement relative to supercell updrafts?*

2) *Do the results from 1) hold true across a range of free tropospheric relative humidity environments?*

We hypothesize that increasing the magnitude of shear, especially across low-to-mid-levels (e.g., 1–6 km), as has typically been done in the prior research summarized above, has two main effects on the relationship between shear, updraft area, and precipitation area in supercells:

- Supercell updrafts amid stronger environmental shear are exposed to stronger low-level storm-relative inflow of CAPE-bearing and moisture-laden air, resulting in wider, less dilute, and stronger updrafts with greater vertical mass flux (akin to processes outlined in Warren et al. 2017 and Peters et al. 2019). Owing to a greater water vapor inflow rate associated with stronger low-level storm-relative inflow and resultant wider updrafts (e.g., Smith et al. 2001; Beatty et al. 2008) amid stronger environmental shear, one might anticipate a commensurate increase in condensate over a wider region. We hypothesize that this results in greater hydrometeor loading, at least during early storm evolution before any substantial downshear advection of hydrometeor mass occurs.

- A greater quantity of condensate (see above) formed within wider updrafts amid stronger shear is advected farther downshear of updrafts by stronger storm-relative winds aloft (Brooks et al. 1994a,b; Trier and Parsons 1995; Rasmussen and Straka 1998; Dennis and Kumjian 2017) than condensate formed within narrower updrafts amid weaker shear, resulting in a wider precipitation area. Furthermore, even though greater hydrometeor loading initially occurs within the updraft amid stronger shear owing to the processes outlined above, more of this hydrometeor mass is transported downshear via strong storm-relative winds aloft, and thus does not greatly reduce maximum updraft vertical velocities.

We hypothesize that the main impact of these two effects – especially the second effect listed above – is to reduce the fraction of condensate produced within updrafts falling to the ground as precipitation (i.e., a substantial fraction of condensate evaporates or sublimates before reaching the surface). Some studies have found that supercells tend to have some of the lowest precipitation efficiencies of all modes of deep convection (Marwitz 1972; Foote and

Accepted for publication in *Monthly Weather Review*. DOI 10.1175/MWR-D-23-0166.1.

Fankhauser 1973; Browning 1977; Jo and Lasher-Trapp 2022, 2023); however, other studies have found just the opposite (Smith et al. 2001; Duda and Gallus 2010; Hitchens and Brooks 2013; Nielsen and Schumacher 2018, 2020).

To address these research questions and test these hypotheses, we conducted and analyzed a suite of idealized numerical simulations of supercells within vertically varying shear and moisture environments that are held constant over time. Shear magnitude was systematically varied over different atmospheric layers while using the same thermodynamic profile. Additional simulations were then conducted with different moisture profiles to test the sensitivity of the results for the control thermodynamic environment to variations in free troposphere RH. The bulk effects of these fixed-in-time systematic shear and moisture variations on supercell updraft characteristics and hydrometeor distributions is main focus of this study.

2. Data and methods

a. Idealized numerical model simulations

To address our research questions and hypotheses, we conducted a suite of idealized supercell simulations using Cloud Model 1 (CM1; Bryan and Fritsch 2002) version 20.3. Most of the specifications for our simulations are listed in Table 1. Each simulation was integrated for 3 h with model output saved every 10 min.

Attribute	**Value/setting**
Fully compressible	Yes
Initial balance setting for 3-D pressure field	Hydrostatic
Horizontal grid spacing	250 m
Vertical grid spacing	Stretched vertical grid between 4–13 km; constant at 50 m below 4 km and at 250 m above 13 km
Vertical coordinate	Height (m)
Number of x, y, z grid points	900 x 900 x 168
Domain size	225 x 225 x 20 km^3
Large time step	5 s
Top and bottom LBC	Free slip

Accepted for publication in *Monthly Weather Review*. DOI 10.1175/MWR-D-23-0166.1.

LBC for domain sides	Open radiative (Durran and Klemp 1983)
Convection initiation technique	Single +3 K warm bubble with a horiz. radius of 10 km and a vert. radius of 1.4 km
u-move; v-move	0.0 m s^{-1}; -6.7 m s^{-1}
Microphysics scheme	Morrison two-moment with hail set as the rimed ice category (Morrison et al. 2009)
Subgrid turbulence scheme	TKE scheme (Deardorff 1980)
Rayleigh damping	Applied above 15 km
Longwave radiation	Off
Shortwave radiation	Off
Surface fluxes	Off
Coriolis acceleration	Off
Include initial random potential temperature perturbations?	Yes; +/- 0.25 K domain-wide

Table 1. Summary of the CM1 configuration. LBC = lateral boundary condition. A weblink to a copy of the namelist.input file can be found in the Data Availability Statement section.

The thermodynamic environment for the control (CTRL) simulations is a modified version of the Weisman and Klemp (1982) sounding (black lines in Fig. 1) with a surface water vapor mixing ratio set to 14 g kg^{-1}, resulting in surface-based CAPE around 1725 J kg^{-1} and surface-based CIN around -50 J kg^{-1} (see red line in Fig. 1 which was computed using MetPy; Unidata 2021). The vertical moisture profile for the CTRL simulations was altered by reducing the RH above 750 hPa, or roughly 2.5 km, by 50% of the original Weisman-Klemp vertical RH profile (black dashed line in Fig. 1). This alteration to the original Weisman-Klemp vertical RH profile better approximates typical severe weather environments found across regions such as the U.S. Great Plains (e.g., Fig. 5 from Rasmussen and Straka 1998; Figs. 7 and 12 from Parker 2014). Two additional vertical moisture profiles were then created by altering the CTRL RH profile to mimic either especially moist or especially dry free tropospheric environments (e.g., Fig. 8 from Nixon et al. 2023). To achieve these variations in free tropospheric RH, the CTRL RH profile was either increased by 50% (MOIST; green dashed line in Fig. 1) or decreased by 25% (DRY; brown dashed line in Fig. 1) above 750 hPa, or roughly 2.5 km, while CAPE, CIN, and EIL depths were largely unchanged (Table 2).

Accepted for publication in *Monthly Weather Review*. DOI 10.1175/MWR-D-23-0166.1.

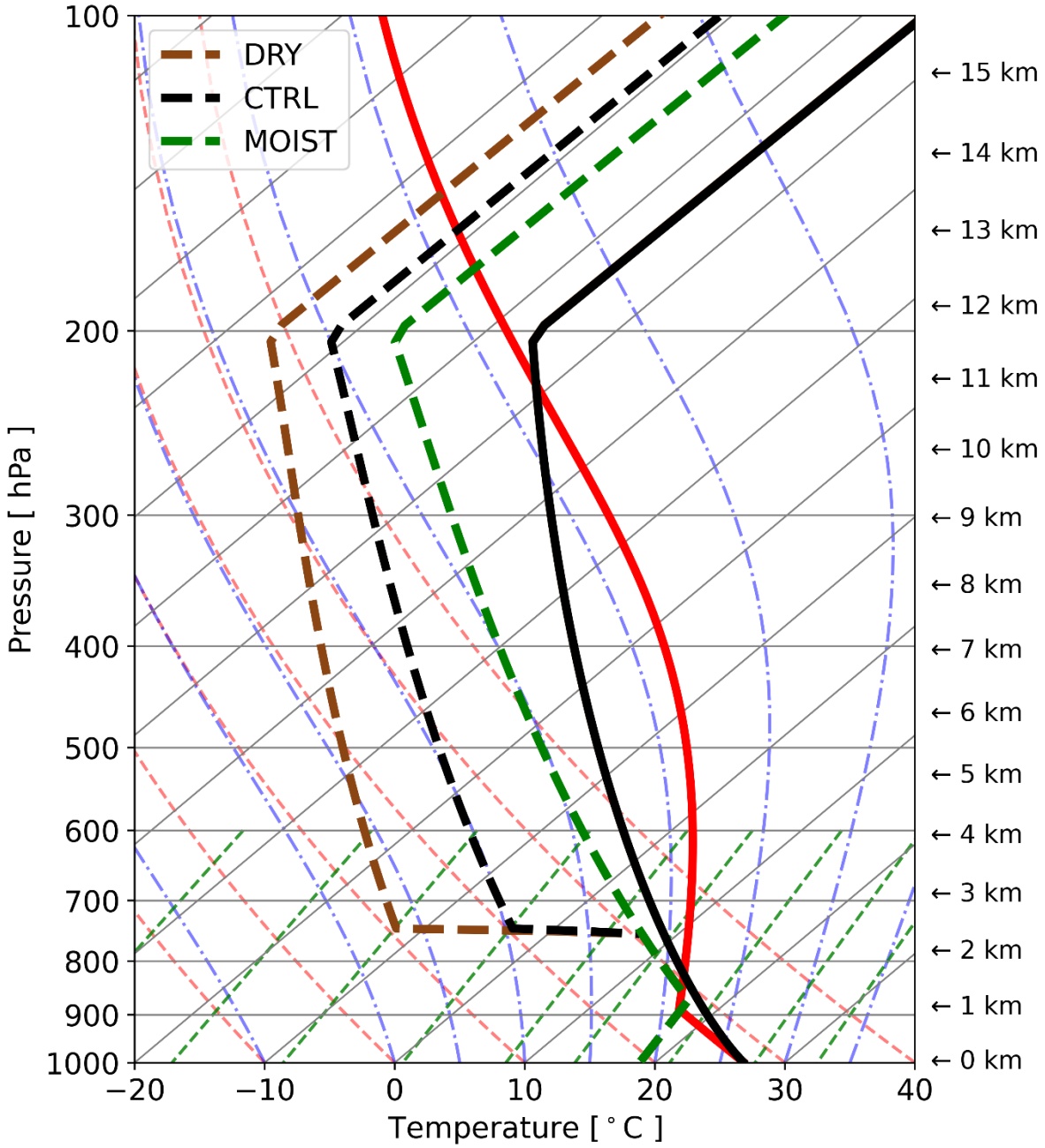

Fig. 1. CM1 input soundings plotted on a skew-*T* log-*P* diagram. The black solid line is temperature (°C) and the dashed brown, black, and green lines are dewpoint temperature (°C) for the DRY, CTRL, and MOIST simulations, respectively. The red solid line is the temperature (°C) of a parcel lifted from the surface. Heights above ground level are listed along the right-hand-side of the diagram.

	SBCAPE [J kg^{-1}]	MLCAPE [J kg^{-1}]	MUCAPE [J kg^{-1}]	SBCIN [J kg^{-1}]	MLCIN [J kg^{-1}]	MUCIN [J kg^{-1}]	EIL depth [m]
DRY	2141	2388	2724	-47	-21	0	2450
CTRL	2114	2361	2697	-47	-21	0	2450

Accepted for publication in *Monthly Weather Review*. DOI 10.1175/MWR-D-23-0166.1.

MOIST	2061	2307	2643	-47	-21	0	3100

Table 2. Summary of the thermodynamic parameters for the CM1 input soundings shown in Fig. 1 computed using SHARPpy (Blumberg et al. 2017). SB = surface-based; ML = 100-hPa mixed-layer; MU = most-unstable; EIL = effective inflow layer.

	0–1 km shear [m s^{-1}]	**1–6 km shear [m s^{-1}]**	**6–12 km shear [m s^{-1}]**
DRY	10 (LL10); 20 (LL20)	25 (ML25); 50 (ML50)	0 (UL00); 25 (UL25)
CTRL	10 (LL10); 20 (LL20)	25 (ML25); 50 (ML50)	0 (UL00); 25 (UL25)
MOIST	10 (LL10); 20 (LL20)	25 (ML25); 50 (ML50)	0 (UL00); 25 (UL25)

Table 3. Summary table of the CM1 simulations along with the naming conventions in the parentheses. Additional sensitivity simulations with corresponding naming conventions are described in the text.

Bulk wind differences/shear magnitudes were systematically varied in the simulations for the sideways "L"-shaped hodograph (Fig. 2; Chavas and Dawson 2021; Peters et al. 2022b,c,d) characteristic of supercell environments (e.g., Fig. 12 from Markowski et al. 2003; Figs. 7 and 12 from Parker 2014) to produce a wide range of supercell sizes and strengths. We chose to vary bulk wind differences/shear magnitudes over three distinct layers: 0–1, 1–6, and 6–12 km. The 0–1 km layer was chosen since this typically spans the boundary layer/EIL and is found below the sharp "kink" in the "L"-shaped hodographs that typify supercell environments. The 1–6 km layer was chosen since this layer spans a majority of the layer traditionally considered in supercell forecasting parameters (i.e., 0–6 km layer) and idealized supercell simulations along with the fact that most of the air in the troposphere resides below 6 km. Lastly, the 6–12 km layer was chosen since this is the layer that is generally thought to be important for near-storm-top "venting" and downshear advection of hydrometeor mass within supercells, and that numerous previous idealized supercell simulation studies have traditionally completely ignored shear effects above 6 km.

Between 0–1 km (low-level, or "LL" hereafter), the u-wind component is constant while the v-wind component linearly increases in magnitude (green lines in Fig. 2). Between

Accepted for publication in *Monthly Weather Review*. DOI 10.1175/MWR-D-23-0166.1.

1–6 km (mid-level[1], or "ML" hereafter), the u-wind component linearly increases in magnitude while the v-wind component is constant (red lines in Fig. 2). Lastly, between 6–12 km (upper-level, or "UL" hereafter), the u-wind component linearly increases in magnitude while the v-wind component is constant (cyan lines in Fig. 2). We chose 2 different LL (10 and 20 m s^{-1}), ML (25 and 50 m s^{-1}), and UL (00 and 25 m s^{-1}) shear magnitudes based upon typical values noted in previous observational supercell studies, with the larger of the two LL, ML, and UL shear magnitudes on the higher end of the observed spectrum (e.g., Figs. 3 and 9 from Rasmussen and Blanchard 1998; Figs. 6–8 from Rasmussen and Straka 1998; Fig. 12 from Markowski et al. 2003; Table 2 and Figs. 8–9 from Thompson et al. 2003; Figs. 8 and 10 from Thompson et al. 2007). Four additional simulations (not shown) were conducted as per suggestion from one of the reviewers in which we tested two additional LL (25 and 45 m s^{-1}) and ML (10 and 25 m s^{-1}) shear magnitudes; however, since half of these simulations failed to produce sustained isolated supercellular deep convection, these simulations were not analyzed further. The shear layer depths and range of shear magnitudes differ among LL, ML, and UL to limit the range of shear conditions tested to those that produce supercells. An example of our naming convention for the simulations is LL10_ML25_UL00_CTRL, which denotes bulk wind difference magnitudes of 10 m s^{-1}, 25 m s^{-1}, and 0 m s^{-1} over the 0–1, 1–6, and 6–12 km layers, respectively, for the control simulation vertical moisture/RH profile (Table 3).

[1] While it is recognized that the lower portion of this 1–6 km layer is typically not described as mid-level, we retain the usage of the term mid-level when describing the 1–6 km layer to differentiate between the three different shear layers in the simulations.

Accepted for publication in *Monthly Weather Review*. DOI 10.1175/MWR-D-23-0166.1.

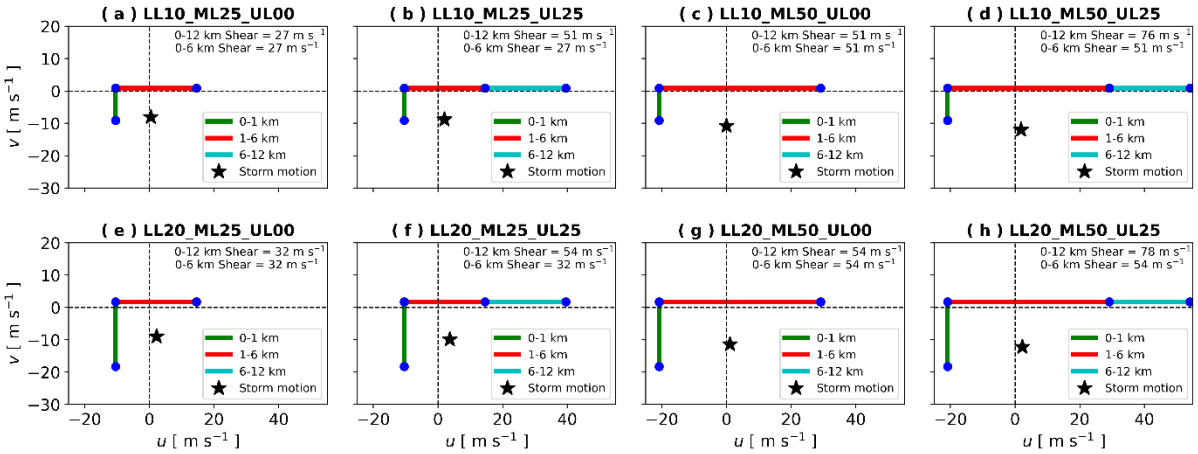

Fig. 2. CM1 input vertical wind profiles plotted on hodographs. Winds are plotted in m s^{-1}. The green, red, and cyan solid lines are the 0–1, 1–6, and 6–12 km vertical layers, respectively, with blue dots demarcating the 0, 1, 6, and 12 km heights. The black stars denote the 90–180 min average storm motions using the right-moving supercell updraft tracking algorithm discussed in section 2b. Storm-relative winds at different heights can be visualized by drawing vectors from these black stars to any of the blue dots on the hodographs. Lastly, 0–6 and 0–12 km bulk vertical wind shear magnitudes are listed in m s^{-1} in the upper right-hand-corner of each panel.

b. Tracking the dominant right-moving supercell

The first step in the analysis of the simulations was to isolate and track the dominant right-moving supercell in each simulation. We restricted our analysis to the 90–180 min output timeframe, which is the time period following storm splitting that occurs in each simulation and is the time period when the right-moving supercells are relatively quasi-steady state and isolated from any nearby deep convection. Storm splitting was visually identified via inspection of lowest-model-level (i.e., 0.025 km) reflectivity animations (Fig. S1). To isolate and track the dominant right-moving supercell updraft in each simulation, the largest contiguous mid-level (5.05 km) core updraft object (i.e., contiguous grid points with vertical velocity ≥ 20 m s^{-1}) was first calculated and saved at each 10-min output time. Next, the *x*- and *y*- locations of the centroid of this largest core updraft object was calculated using SciPy's "ndimage.measurements.center_of_mass" function in Python (https://docs.scipy.org/doc/scipy-0.14.0/reference/generated/scipy.ndimage.measurements.center_of_mass.html) and saved at each 10-min output time. Finally, a 1-D Gaussian smoother function in Python (https://docs.scipy.org/doc/scipy/reference/generated/scipy.ndimage.gaussian_filter1d.html) was applied to these *x*- and *y*- locations using a standard deviation of the Gaussian kernel (i.e., sigma) equal to 1.

Accepted for publication in *Monthly Weather Review*. DOI 10.1175/MWR-D-23-0166.1.

c. Creating composites around the dominant right-moving supercell

Using the smoothed *x*- and *y*- locations for the right-moving supercell in each simulation, a sub-domain was defined around each of these points that was 200 grid points (50 km) to the north, 355 grid points (88.75 km) to the east, 100 grid points (25 km) to the south, and 245 grid points (61.25 km) to the west to create a total sub-domain size of 600 grid points x 300 grid points or 150 x 75 km^2 which completely captured and isolated the right-moving supercell in each simulation while avoiding nearby ancillary deep convection. Once each of these new sub-domains was defined, output fields, such as reflectivity, buoyancy (relative to a reference or initial state), and vertical velocity, among others, were saved at each 10-min output time and averaged over the 90–180 min output timeframe within each sub-domain to create composite fields. Model fields, which were additionally analyzed at various specific output times between the 90–180 min timeframe, fully embodied the 90–180 min composites (not shown).

d. Creating composite vertical profiles of quantities within and outside core updrafts

Vertical profiles of quantities (e.g., vertical velocity, hydrometeor mass[2], etc.) were defined both within (grid points with vertical velocity ≥ 20 m s^{-1}) and outside (grid points with vertical velocity < 20 m s^{-1}) core updrafts[3] at each 10-min output time at each model vertical level within the right-moving supercell sub-domain over the 90–180 min output timeframe. These profiles were then averaged over the 90–180 min output timeframe to create composite profiles.

e. Creating composite west-to-east oriented vertical cross sections

West-to-east oriented vertical cross sections were created and saved at each 10-min output time by calculating the maximum values of quantities in the *y*-direction at every *x*- and *z*- grid point across the right-moving supercell sub-domain. These new 3-D arrays were then

[2] Hydrometeor mass was calculated by summing the mixing ratios of rain, snow, hail, cloud ice, and cloud liquid.

[3] Results were consistent across various core updraft vertical velocity thresholds tested, such as 10 m s^{-1} and 30 m s^{-1}.

Accepted for publication in *Monthly Weather Review*. DOI 10.1175/MWR-D-23-0166.1.

averaged over the 90–180 min output timeframe to create composite west-to-east oriented vertical cross sections.

f. Calculating the horizontal separation between the updraft core and reflectivity core

To quantify the horizontal separation between the updraft core and reflectivity core, we first identified the largest contiguous near-surface (0.025 km) core reflectivity object (i.e., contiguous grid points with reflectivity ≥ 50 dBZ). The near-surface core reflectivity objects were tracked in the same way as the mid-level core updraft objects. Finally, the horizontal distance between these smoothed *x*- and *y*- core updraft and core reflectivity locations was calculated and saved at each 10-min output time between the 90–180 min output timeframe.

g. Calculating the water vapor budget

Using built-in software in CM1 (i.e., setting "*output_qvbudget = 1*" in the namelist.input file), the water vapor budget was calculated in-line with the model integration at each model time step. Instantaneous process rates, such as evaporation of rain plus melting snow/hail and sublimation of cloud ice, snow, and hail, among other process rates, were saved at each 10-min output time. These process rates were analyzed across the right-moving supercell sub-domain and averaged over the 90–180 min timeframe to create composite fields, such as horizontal plan views, vertical cross sections, and vertical profiles.

h. Quantifying entrainment-driven dilution within core updrafts

To quantify entrainment-driven dilution in the simulations, composite vertical profiles of moist static energy (MSE) within core updrafts were calculated across the right-moving supercell sub-domain between the 90–180 min output timeframe. MSE was calculated using temperature dependent latent heats (eq. 6 in Romps 2016; eq. 5 in Peters and Chavas 2021; eq. 14 in Peters et al. 2022a). Since MSE is approximately adiabatically conserved in undiluted core updrafts of deep convection (Kiefer 1941; Riehl and Malkus 1958; Kreitzberg 1964; Zhang and McFarlane 1991; Zhang 2009; Peters et al. 2020a) – which is common in numerically simulated supercells (e.g., Peters et al. 2019) – it can be used, at least as a proxy, to quantify entrainment-driven dilution. Larger values of MSE in core updrafts across most of the troposphere (where core MSE is greater than the environmental MSE) indicates reduced entrainment-driven dilution.

Accepted for publication in *Monthly Weather Review*. DOI 10.1175/MWR-D-23-0166.1.

i. Quantifying differences between the three weak and strong shear groups

To quantify the differences between the weak and strong shear magnitude simulation groups across the three different layers (i.e., LL, ML, and UL), the percent difference between the weak and strong shear simulation groups was computed. Percent differences were determined by: $\frac{\overline{\textbf{\textit{Strong Shear Group}}} - \overline{\textbf{\textit{Weak Shear Group}}}}{\overline{\textbf{\textit{Strong Shear Group}}}} \times \mathbf{100}$, where an overbar denotes the average across a group of either weak or strong shear simulations for LL, ML, and UL. Percent differences were computed for both time series and composite vertical profile plots shown in section 3. Positive percent differences indicate that the variable being analyzed was larger in the stronger shear group for that particular shear layer whereas negative percent differences indicate that the variable being analyzed was larger in the weaker shear group for that particular shear layer.

j. Additional sensitivity simulations

All of the weak (ML25) and strong (ML50) mid-level shear simulations using LL20 and UL25 with the drier (DRY), control (CTRL), and moister (MOIST) free troposphere background environment were re-run for two additional sensitivity tests. The first sensitivity test involved changing the microphysics parameterization scheme from the Morrison two-moment scheme (MORR; Morrison et al. 2009) to the National Severe Storms Laboratory (NSSL) two-moment scheme (Mansell et al. 2010; Mansell and Ziegler 2013), which includes the concurrent representation of both graupel and hail ice species, whereas the Morrison two-moment scheme only represents one or the other (hail was chosen for this study). The second sensitivity test included modifying the specified cloud droplet number concentration in the Morrison two-moment scheme (i.e., setting "*ndcnst*" in the namelist.input file) from the default concentration of 250 cm^{-3} to either a low, pristine, maritime concentration (50 cm^{-3}) or a high, polluted, continental concentration (1000 cm^{-3}) to alter the amount of hydrometeor loading within the simulations. The results from these two sets of additional sensitivity simulations are presented in Appendices A and B.

3. Results

a. Control simulations

Accepted for publication in *Monthly Weather Review*. DOI 10.1175/MWR-D-23-0166.1.

Analysis of the plan view composites for the CTRL simulations reveal that as shear increases, especially mid-level shear, mid-level updraft area and near-surface reflectivity area both increase (Fig. 3; compare left four panels with right four panels). Furthermore, the near-surface cold pool area[4] also increases with increasing mid-level shear (Fig. 3) in accord with increasing near-surface precipitation rate and area, along with surface precipitation accumulation (Figs. 4-5). Percent differences between the ML25 and ML50 near-surface precipitation rates and precipitation accumulations are fairly consistent across the 90–180 min output timeframe and generally range between 40–70% (red lines in Fig. 5c,d) whereas percent differences between UL00 and UL25 were generally between 5–25% (cyan lines in Fig. 5c,d). Interestingly, the percent differences between LL10 and LL20 were relatively large with values generally ranging between -25% and -75% across the 90–180 min output timeframe (green lines in Fig. 5c,d). This indicates that as low-level shear magnitude increased, near-surface precipitation rates and precipitation accumulations decreased, which misaligns with the results from studies such as Nielsen and Schumacher (2018, 2020). Reasons for these trends in near-surface precipitation rates and precipitation accumulations due to changes in low-level shear magnitude are unclear and are beyond the scope of the present study.

Alternatively, mid-level updraft area and near-surface reflectivity area exhibit comparatively less sensitivity to changes in either low-level (Fig. 3; compare top row and bottom row) or upper-level (Fig. 3; compare adjacent left and right panels) shear magnitudes. One specific impact of changes in upper-level shear is that the downshear near-surface reflectivity area is elongated in the west-to-east direction in the stronger upper-level shear (UL25) simulations (Fig. 3; compare adjacent left and right panels) owing to stronger storm-relative winds aloft (e.g., see black stars denoting 90–180 min average simulated storm motions in Fig. 2). This trend for enhanced downshear elongation of the near-surface reflectivity area is also evident for the stronger 0–12 km bulk shear magnitudes (compare Fig. 3a,e and Fig. 3b,f and also Fig. 3c,g and Fig. 3d,h) listed in Fig. 2.

[4] Defined using grid points with lowest-model-level (0.025 km) buoyancy < -0.05 m s^{-2}.

Accepted for publication in *Monthly Weather Review*. DOI 10.1175/MWR-D-23-0166.1.

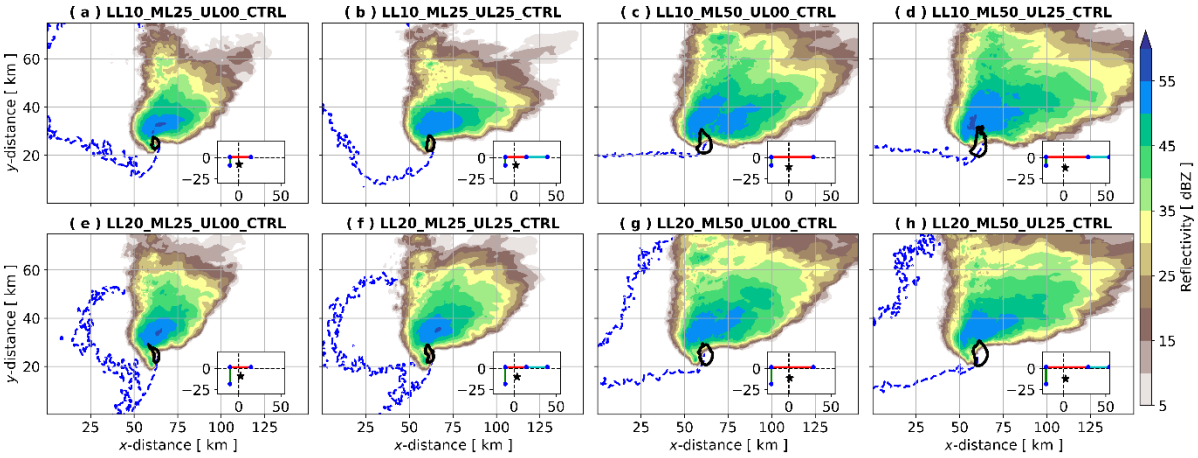

Fig. 3. Plan view 90–180 min composite[5] of near-surface (0.025 km) radar reflectivity (shaded; dBZ), mid-level (5.05 km) vertical velocity (black contour = 20 m s^{-1}), and near-surface (0.025 km) buoyancy (blue contour < -0.05 m s^{-2}). The CM1 input vertical wind profiles plotted on hodographs from Fig. 2 are shown in the lower right-hand-side of each panel.

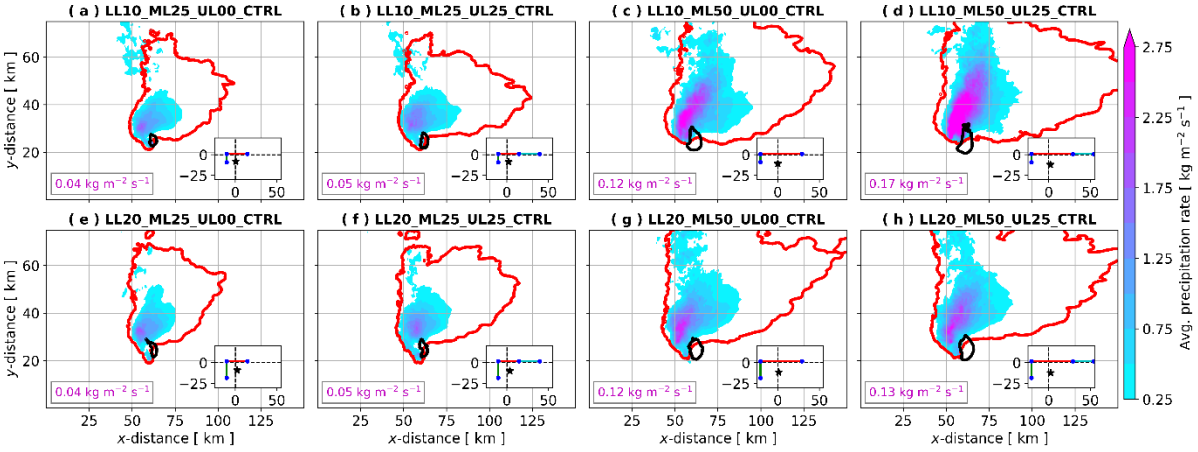

Fig. 4. Plan view 90–180 min composite of near-surface (0.025 km) reflectivity (red contour = 20 dBZ) and precipitation rate (shaded; kg m^{-2} s^{-1}). The area-averaged precipitation rate is shown in magenta text in the lower left-hand-side of each panel and the CM1 input vertical wind profiles plotted on hodographs from Fig. 2 are shown in the lower right-hand-side of each panel. Area-averages were computed across the entire right-moving supercell sub-domain as shown here and discussed in section 2c.

[5] Composite refers to time averages over the 90–180 min timeframe here and throughout the manuscript.

Accepted for publication in *Monthly Weather Review*. DOI 10.1175/MWR-D-23-0166.1.

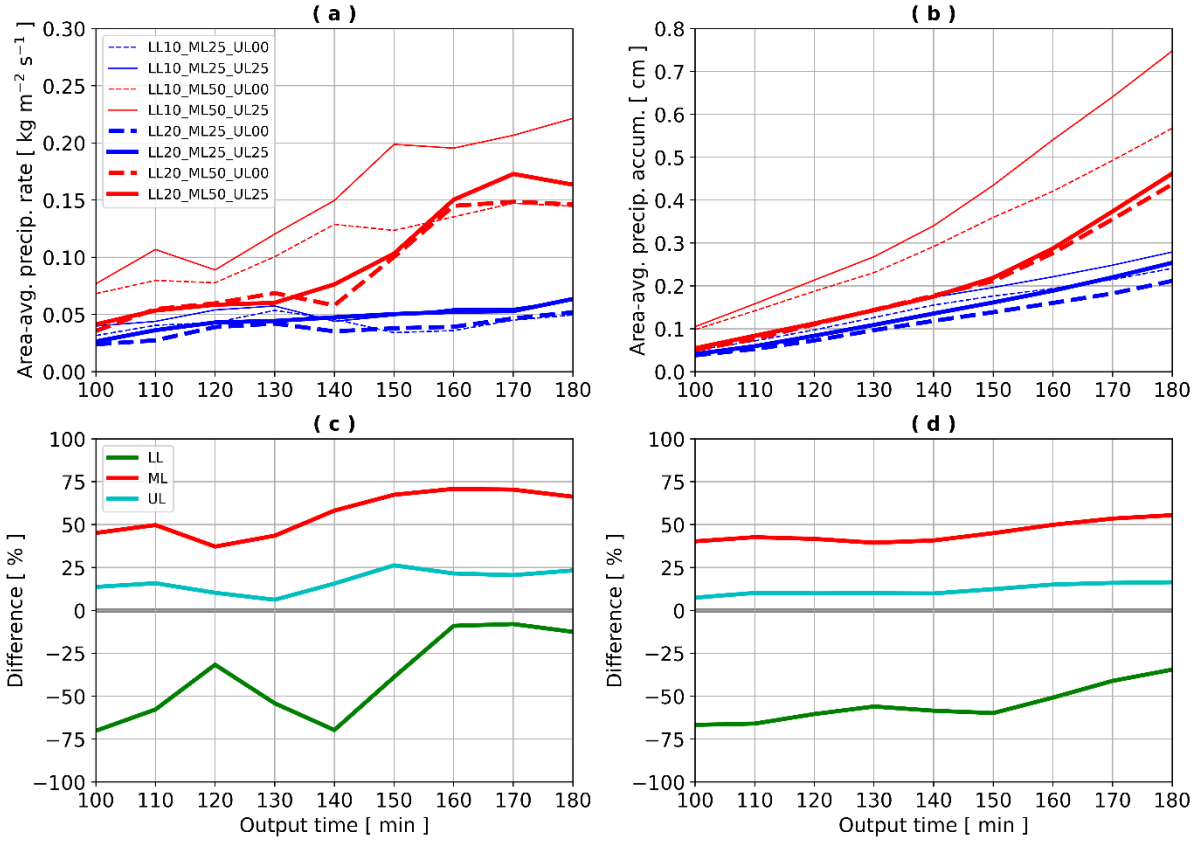

Fig. 5. Time series (in min) of (a) area-averaged precipitation rate (kg m^{-2} s^{-1}) and (b) area-averaged precipitation accumulation (cm) for CTRL simulations. Area-averages were computed across the entire right-moving supercell sub-domain as discussed in section 2c. Panels (c) and (d) denote the differences (expressed as a %; please see section 2i) between all of the strong and weak LL (green), ML (red), and UL (cyan) shear simulations.

Time series of maximum mid-level (5.05 km) core updraft area (Fig. 6a) and near-surface (0.025 km) core reflectivity area (Fig. 6b) confirms that these quantities are most sensitive to changes in mid-level shear magnitude, with stronger mid-level shear yielding wider mid-level updrafts, in agreement with several studies (e.g., Dennis and Kumjian 2017; Trapp et al. 2017; Warren et al. 2017, Marion and Trapp 2019; Peters et al. 2019; Mulholland et al. 2020; Peters et al. 2020b). Furthermore, stronger mid-level shear, and thus stronger low-level storm-relative inflow (e.g., see black stars denoting 90–180 min average simulated storm motions in Fig. 2), leads to larger near-surface reflectivity areas. Percent differences between the ML25 and ML50 maximum mid-level core updraft areas and near-surface core reflectivity areas are fairly consistent across the 90–180 min output timeframe and generally range between 40–70% (red lines in Fig. 6c,d). Percent differences between LL10 and LL20 generally range between -40% and 20% (green lines in Fig. 6c,d) whereas percent differences between UL00 and UL25 generally range between 5–35% (cyan lines in Fig. 6c,d).

Accepted for publication in *Monthly Weather Review*. DOI 10.1175/MWR-D-23-0166.1.

Core updraft area is not only larger at mid-levels with stronger mid-level shear, but is uniformly larger throughout most of the depth of the troposphere (Fig. 7a). Percent differences between the ML25 and ML50 core updraft area composite vertical profiles generally range between 60–80% above the freezing level, or above ~3.5 km (red line in Fig. 7e). Percent differences between LL10 and LL20 generally range between -25% and 25% above the freezing level, or above ~3.5 km (green line in Fig. 7e). Percent differences between UL00 and UL25 generally range between -10% and 10% above the freezing level, or above ~3.5 km (cyan line in Fig. 7e). Composite vertical profiles of maximum updraft and downdraft strengths reveal the same bifurcation between the weak (ML25; blue lines in Fig. 8a) and strong (ML50; red lines in Fig. 8a) mid-level shear simulations. Stronger mid-level shear leads to stronger low-to-mid-level updrafts (Fig. 8a; right side) and stronger downdrafts throughout the entire troposphere than weaker mid-level shear (Fig. 8a; left side), with percent differences between the ML25 and ML50 simulations of up to 20% around the freezing level (~3.5 km) for updrafts (red solid line in Fig. 8d) and around 20–30% between the freezing level (~3.5 km) and 12 km for downdrafts (red dashed line in Fig. 8d). Percent differences between UL00 and UL25 were relatively small for both updrafts and downdrafts (cyan lines in Fig. 8d), whereas percent differences between LL10 and LL20 for updrafts reached a maximum between 25–30% around 2 km (green solid line in Fig. 8d). These stronger vertical velocities in stronger mid-level shear simulations are consistent with wider core updrafts (Figs. 6a,7a) that are less dilute as indicated by larger core updraft MSE by ~5% between approximately 5–13 km (Figs. 7b,f). Specifically, the stronger low-to-mid-level updrafts (Fig. 8a; right side), especially between 2–8 km, likely also owes to stronger non-linear dynamic perturbation pressure gradient accelerations owing to more rapidly rotating updrafts in the ML50 and LL20 than in the ML25 and LL10 simulations (not shown), in agreement with numerous previous studies (e.g., Coffer and Parker 2015; Nielsen and Schumacher 2018; Peters et al. 2019).

Accepted for publication in *Monthly Weather Review*. DOI 10.1175/MWR-D-23-0166.1.

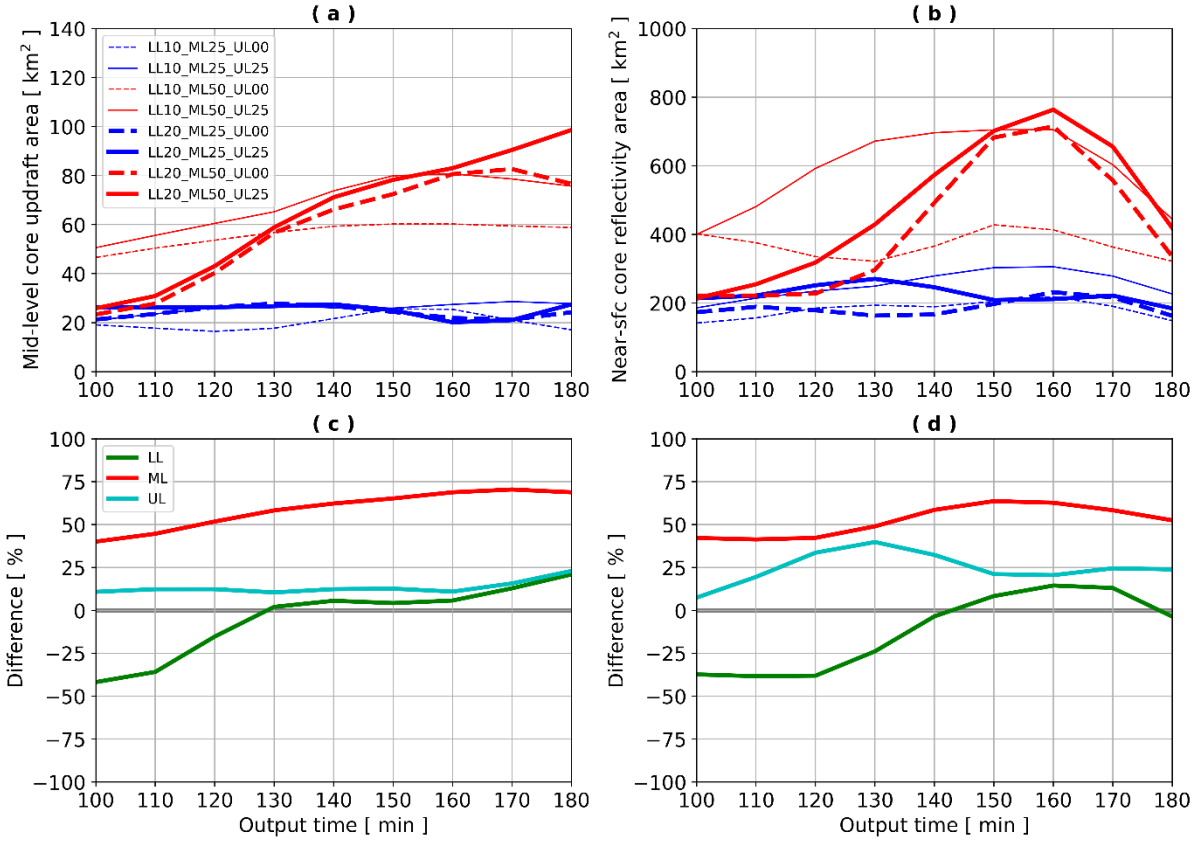

Fig. 6. Time series (in min) of (a) mid-level (5.05 km) core updraft area (km^2) and (b) near-surface (0.025 km) core reflectivity area (km^2) for CTRL simulations. The definitions for core updraft and reflectivity areas are discussed in sections 2b and 2f. Panels (c) and (d) denote the differences (expressed as a %; please see section 2i) between all of the strong and weak LL (green), ML (red), and UL (cyan) shear simulations.

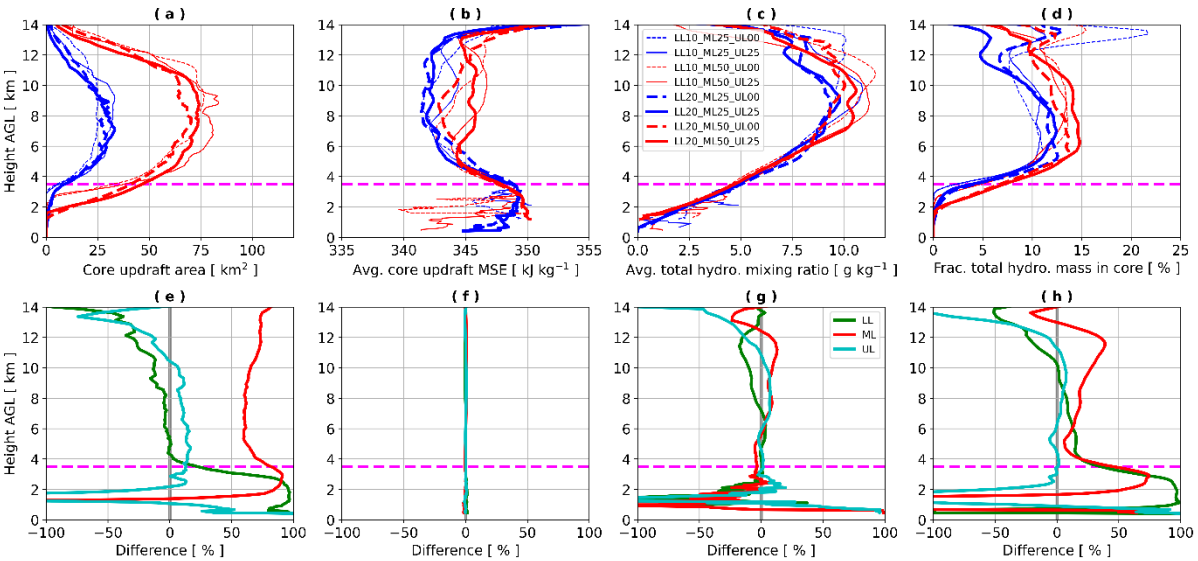

Fig. 7. Vertical profile 90–180 min composites of (a) core updraft area (km^2), (b) average core updraft MSE (kJ kg^{-1}), (c) average hydrometeor mixing ratio within core updrafts (g kg^{-1}), and (d) the fraction (expressed as a percentage) of hydrometeor mass within core updrafts relative to that of the entire right-moving supercell sub-domain for CTRL simulations. Panels (e)–(h) denote the differences (expressed as a %; please see section 2i) between all of the strong and weak LL (green), ML (red), and UL (cyan) shear

Accepted for publication in *Monthly Weather Review*. DOI 10.1175/MWR-D-23-0166.1.

simulations. The horizontal dashed magenta line in each panel is the environmental freezing level (0°C) at approximately 3.5 km.

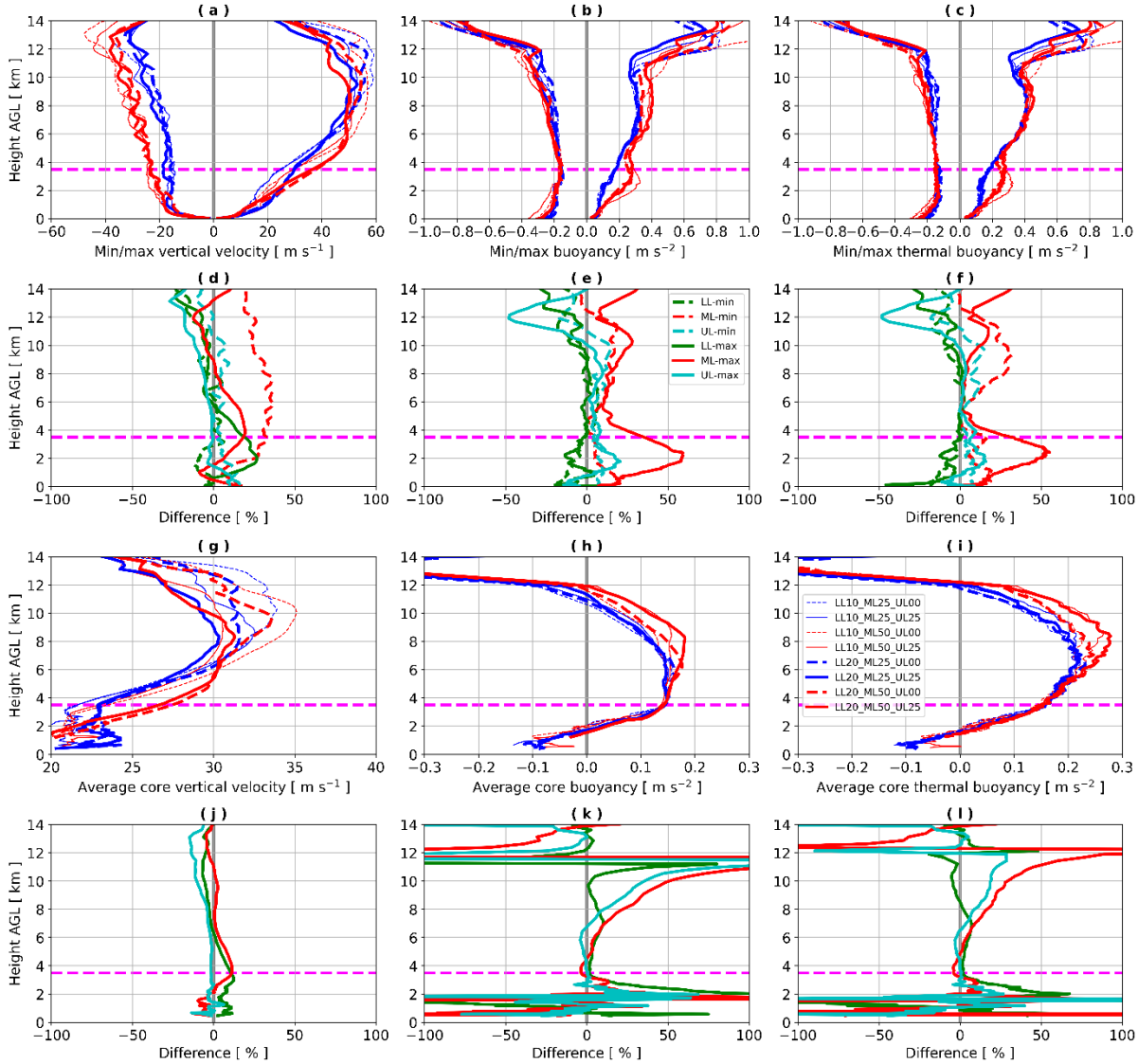

Fig. 8. Vertical profile 90–180 min composites of (a) minimum/maximum vertical velocity (m s^{-1}), (b) minimum/maximum buoyancy (m s^{-2}), (c) minimum/maximum thermal buoyancy (m s^{-2}), (g) average core vertical velocity (m s^{-1}), (h) average core buoyancy (m s^{-2}), and (i) average core thermal buoyancy (m s^{-2}) for CTRL simulations. Panels (d)–(f) and (j)–(l) denote the differences (expressed as a %; please see section 2i) between all of the strong and weak LL (green), ML (red), and UL (cyan) shear simulations. The horizontal dashed magenta line in each panel is the environmental freezing level (0°C) at approximately 3.5 km.

Composite vertical profiles of average hydrometeor mass within core updrafts reveal that increasing mid-level shear leads to greater hydrometeor loading within updrafts, especially between 6–12 km (Fig. 7c), owing to updrafts being wider (Figs. 6a,7a), less dilute (Fig. 7b), and stronger (Fig. 8a; right side). Furthermore, the relative fraction of hydrometeor mass within core updrafts compared to that of the entire right-moving supercell sub-domain is greater in stronger mid-level shear simulations (i.e., ~10% for weaker mid-level shear compared to ~15%

Accepted for publication in *Monthly Weather Review*. DOI 10.1175/MWR-D-23-0166.1.

for stronger mid-level shear), especially between 5–12 km (Fig. 7d). Percent differences between the ML25 and ML50 average hydrometeor mass within core updraft composite vertical profiles generally range between 0–10% across 6–12 km (red line in Fig. 7g). Percent differences between LL10 and LL20 generally range between -15% to 5% across 6–12 km (green line in Fig. 7g) whereas percent differences between UL00 and UL25 generally range between 0–5% across 6–11 km (cyan line in Fig. 7g). Percent differences between the ML25 and ML50 relative fraction of hydrometeor mass within core updrafts compared to that of the entire right-moving supercell sub-domain composite vertical profiles generally range between 10–40% across 5–12 km (red line in Fig. 7h). Percent differences between LL10 and LL20 generally range between -25% and 25% across 5–12 km (green line in Fig. 7h) whereas percent differences between UL00 and UL25 generally range between -5% and 5% across 5–12 km (cyan line in Fig. 7h). This additional hydrometeor mass and loading within core updrafts amid stronger mid-level shear does not greatly reduce maximum buoyancy within core updrafts, however, as revealed by composite vertical profiles of both maximum (Fig. 8b; right side) and average core (Fig. 8h) buoyancy. Instead, maximum buoyancy is greater, especially between 1–4 km and 6–11 km, for stronger mid-level shear simulations (Fig. 8b; right side). Percent differences between the ML25 and ML50 maximum buoyancy within core updrafts composite vertical profiles generally range between 20–60% and 10–30% over the 1–4 km and 6–11 km layers, respectively (red solid line in Fig. 8e). Furthermore, both maximum (Fig. 8c; right side) and average core (Fig. 8i) thermal buoyancy generally mimic the patterns noted with total buoyancy (especially at low-levels) and show an increase in magnitude with increasing mid-level shear owing to wider (Figs. 6a,7a), less dilute (Fig. 7b) core updrafts. Greater hydrometeor loading within the ML50 than in the ML25 supercell core updrafts (Fig. 7c), along with only minor differences in maximum thermal buoyancy at mid-to-upper levels (Fig. 8c; red solid lines in Fig. 8f), may explain the relatively minor (i.e., a few m s^{-1} or less) differences in mid-to-upper level (i.e., 6–12 km) maximum vertical velocities between the ML25 and ML50 simulations (Fig. 8a; right side; red solid line in Fig. 8d). Thus, although there is greater hydrometeor loading within updrafts amid stronger mid-level shear, total buoyancy is still larger than in weaker mid-level shear simulations owing to a compensating effect of larger thermal buoyancy within wider updrafts in stronger mid-level shear simulations.

Hydrometeor mass is also greater outside of core updrafts in the stronger mid-level shear simulations (Fig. 9a). Percent differences between the ML25 and ML50 hydrometeor mass outside of core updraft composite vertical profiles generally range between 50–60%

Accepted for publication in *Monthly Weather Review*. DOI 10.1175/MWR-D-23-0166.1.

across the depth of the troposphere (red line in Fig. 9d). Percent differences between LL10 and LL20 generally range between -30% to -40% across the depth of the troposphere (green line in Fig. 9d) whereas percent differences between UL00 and UL25 generally range between -20% and 20% across the depth of the troposphere (cyan line in Fig. 9d). This greater amount of hydrometeor mass existing outside of core updrafts amid stronger mid-level shear owes to both (1) increasing hydrometeor mass detrainment aloft associated with wider (Figs. 6a,7a) and stronger updrafts (Fig. 8a; right side) that contain a greater concentration of hydrometeor mass (Fig. 7c) and (2) stronger storm-relative winds (e.g., Fig. 2) horizontally displacing some of this increased hydrometeor mass downshear of the updraft (similar to the simulations in Jo and Lasher-Trapp 2022). However, as shown in Fig. 7d and described in the previous paragraph, a smaller overall proportion of hydrometeor mass is being advected out of core updrafts in stronger than weaker mid-level shear simulations owing to greater hydrometeor concentrations in wider updrafts. The horizontal separation distance between the smoothed mid-level core updraft centroid and smoothed near-surface core reflectivity centroid is larger and increases at a faster rate with stronger mid-level shear magnitudes than for weaker mid-level shear magnitudes (Fig. 10). For example, the mean separation distance between the smoothed mid-level core updraft centroid and smoothed near-surface core reflectivity centroid is ~13.8 km for the ML25 simulations (Fig. 10a,b,e,f) compared to ~22.0 km for the ML50 simulations (Fig. 10c,d,g,h), or approximately a percent difference of 37%. Lastly, the mid-to-upper-level (> 5 km) storm-relative wind direction appears most determinative of where the near-surface core reflectivity area is located within supercells (Fig. S2; also see Fig. 2).

Accepted for publication in *Monthly Weather Review*. DOI 10.1175/MWR-D-23-0166.1.

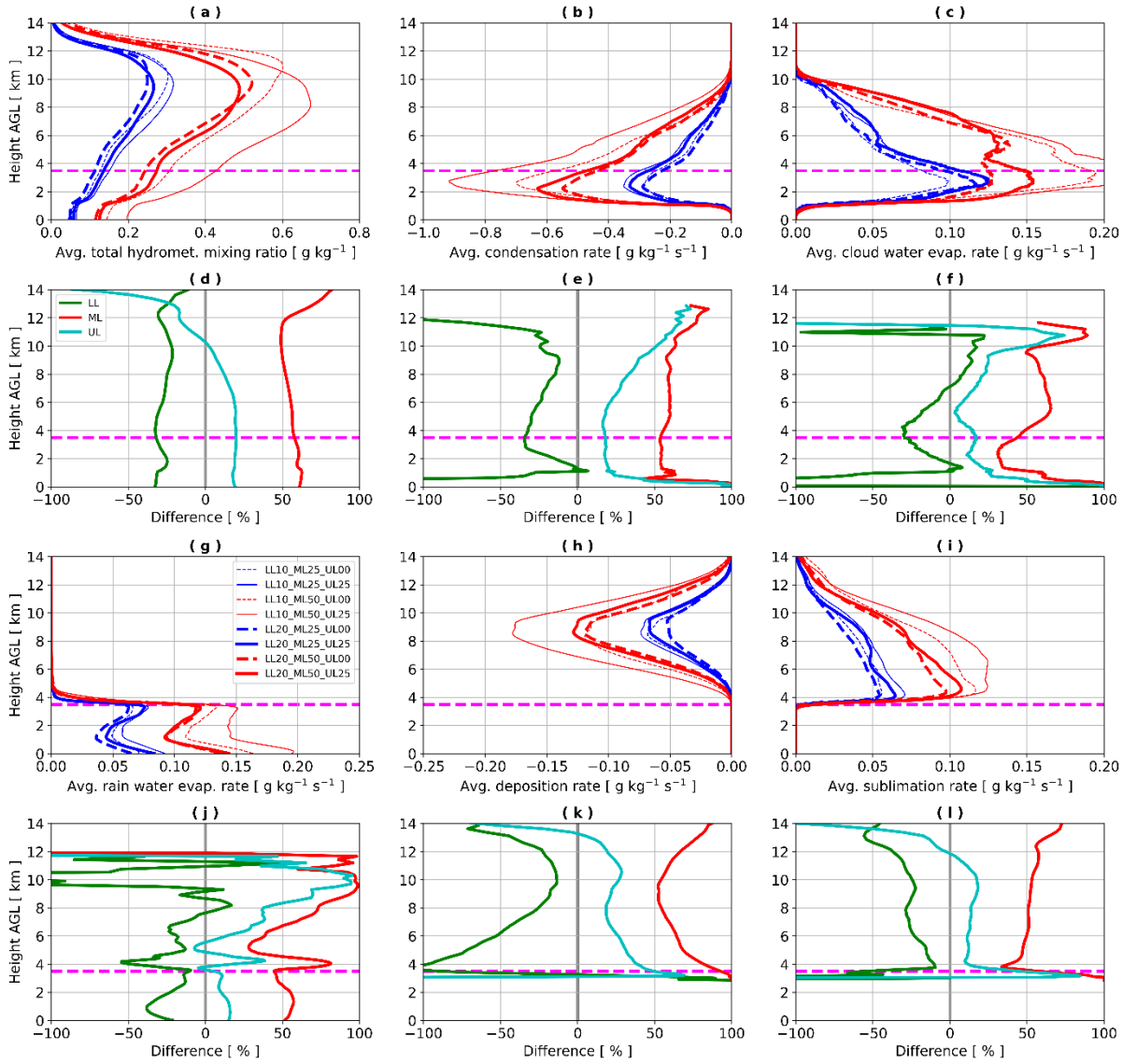

Fig. 9. Vertical profile 90–180 min composites of (a) average hydrometeor mixing ratio outside of core updrafts (g kg^{-1}) and (b–c and g–i) terms in the water vapor budget outside of core updrafts (g kg^{-1} s^{-1}) for CTRL simulations. Panels (d)–(f) and (j)–(l) denote the differences (expressed as a %; please see section 2i) between all of the strong and weak LL (green), ML (red), and UL (cyan) shear simulations. The horizontal dashed magenta line in each panel is the environmental freezing level (0°C) at approximately 3.5 km.

Accepted for publication in *Monthly Weather Review*. DOI 10.1175/MWR-D-23-0166.1.

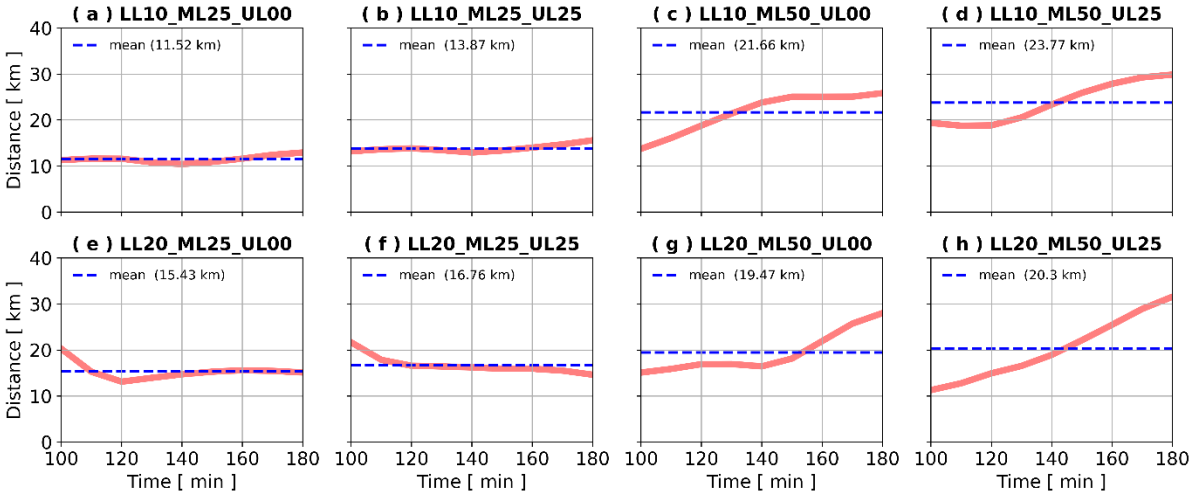

Fig. 10. Time series (in min) of the horizontal separation distance (km) between the smoothed mid-level (5.05 km) core updraft centroid and the smoothed near-surface (0.025) core reflectivity centroid for CTRL simulations. Means are listed and also are denoted as horizontal dashed blue lines in each panel.

Plan view and west-to-east oriented vertical cross section composites of a selection of water vapor budget terms[6] indicate that both rates of sublimation at mid-to-upper levels and evaporation at low-levels increase with stronger mid-level shear (Figs. 11-12). These sublimation and evaporation regions are larger and spread more horizontally downshear in the stronger mid-level shear simulations (Figs. 11-12). In fact, all terms in the water vapor budget are larger in magnitude in the stronger mid-level shear simulations with percent differences between the ML25 and ML50 simulations generally between 30–90% (red lines in Fig. 9e–f and j–l). Greater cloud (Fig. 9c) and rain water (Fig. 9g) evaporation, along with greater sublimation (Fig. 9i), in stronger mid-level shear simulations potentially explains the stronger downdrafts throughout the troposphere in these simulations (Fig. 8a; left side), in addition to hydrometeor loading effects due to the greater hydrometeor mass outside core updrafts (Fig. 9a).

[6]The terms of the water vapor budget are plotted relative to changes in water vapor concentration that they produce, meaning that evaporation (condensation) yields positive (negative) numbers.

Accepted for publication in *Monthly Weather Review*. DOI 10.1175/MWR-D-23-0166.1.

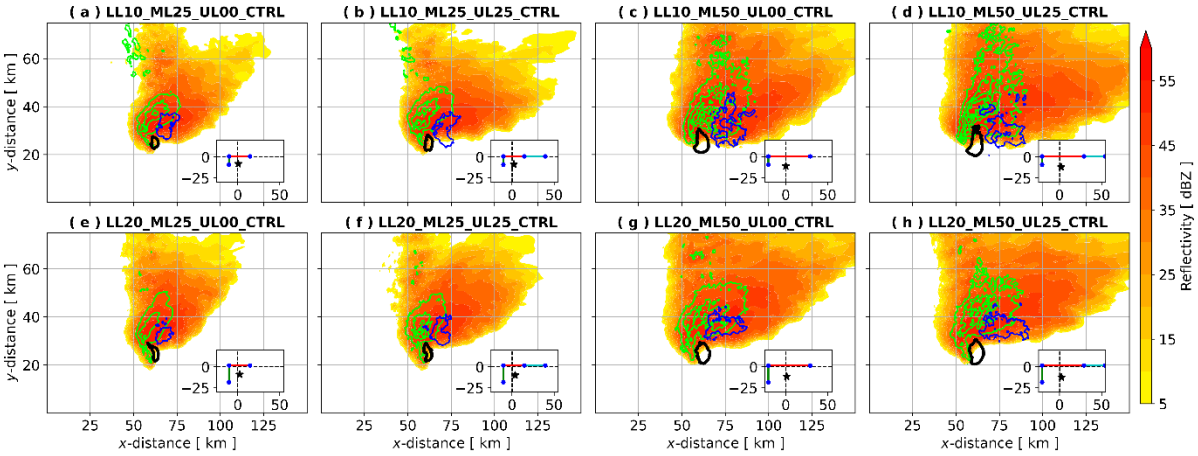

Fig. 11. Plan view 90–180 min composite of near-surface (0.025 km) radar reflectivity (shaded; dBZ), mid-level (5.05 km) vertical velocity (black contour = 20 m s^{-1}), process rates of mid-to-upper level (4.025–11.902 km) sublimation of cloud ice, snow, and hail (blue contours between 0.5–5.5 x 10^6 g kg^{-1} s^{-1} every 1 x 10^6 g kg^{-1} s^{-1}), and low-level (0.025–3.025 km) evaporation of rain plus melting snow/hail (green contours between 0.5–5.5 x 10^6 g kg^{-1} s^{-1} every 1 x 10^6 g kg^{-1} s^{-1}). The CM1 input vertical wind profiles plotted on hodographs from Fig. 2 are shown in the lower right-hand-side of each panel.

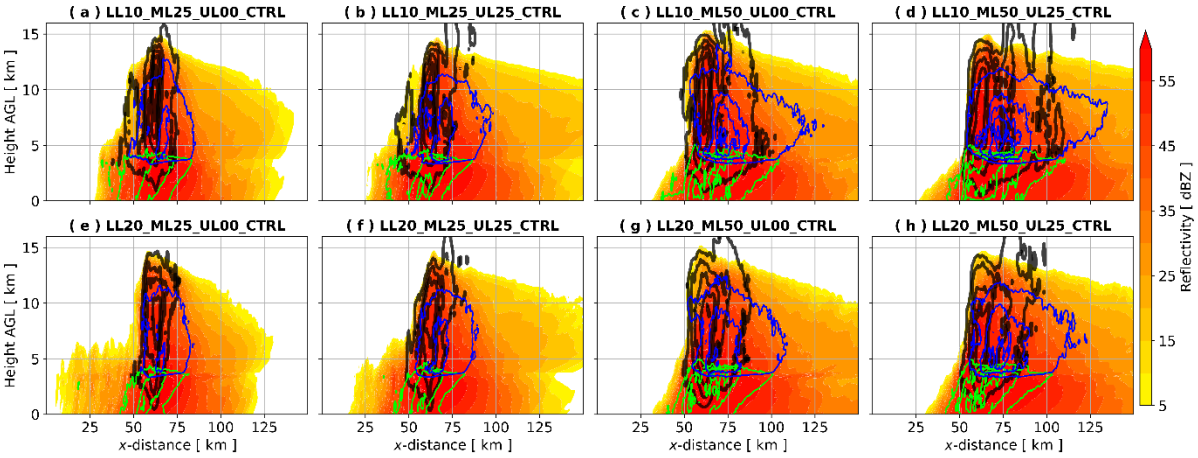

Fig. 12. West-to-east-oriented vertical cross section 90–180 min composite of maximum-in-*y*-direction radar reflectivity (shaded; dBZ), vertical velocity (black contours between 10–70 m s^{-1} every 10 m s^{-1}), process rates of sublimation of cloud ice, snow, and hail (blue contours between 1–22 x 10^6 g kg^{-1} s^{-1} every 3 x 10^6 g kg^{-1} s^{-1}), and evaporation of rain plus melting snow/hail (green contours between 1–22 x 10^6 g kg^{-1} s^{-1} every 3 x 10^6 g kg^{-1} s^{-1}).

To summarize thus far, changes in mid-level shear magnitudes have a strong impact on mid-level updraft area (and updraft area across all heights), near-surface reflectivity area, near-surface precipitation area, near-surface precipitation rate, and near-surface cold pool area. These impacts are larger than those from changes to the low-level and upper-level shear magnitudes, with some minor exceptions as noted earlier (e.g., Fig. 8a; right side; green solid line in Fig. 8d). Stronger shear across the 1–6 km layer leads to larger values of all of these quantities. Furthermore, stronger mid-level shear leads to greater hydrometeor loading within updrafts and a higher relative fraction of hydrometeor mass existing within core updrafts. Wider, less dilute updrafts amid stronger mid-level shear yields greater thermal buoyancy

Accepted for publication in *Monthly Weather Review*. DOI 10.1175/MWR-D-23-0166.1.

within core updrafts that compensates for this increase in hydrometeor loading, resulting in greater total buoyancy within core updrafts in stronger mid-level shear. Owing to the stronger storm-relative winds, along with greater detrainment of hydrometeor mass aloft owing to wider and stronger updrafts that contain more hydrometeor mass in stronger mid-level shear simulations, there is more hydrometeor mass existing outside of core updrafts. This results in greater sublimation and evaporation rates outside of core updrafts potentially explaining the stronger downdrafts across the depth of the troposphere in these stronger mid-level simulations. Next, we test if these results are consistent across a range of free tropospheric RH environments.

b. Moist versus dry free troposphere RH simulations

To address our second research question regarding the influence of free troposphere RH (see the Introduction), we re-ran all 8 CTRL simulations with either a drier (DRY) or a moister (MOIST) free troposphere RH (brown and green dashed lines, respectively, in Fig. 1). The plan view composites for the DRY and MOIST simulations reveal similar trends as in the CTRL simulations; as shear increases, especially mid-level shear, mid-level updraft area and near-surface reflectivity area both increase along with near-surface cold pool area (Figs. 13-14; compare left four panels with right four panels). Increasing free tropospheric RH also leads to larger mid-level updraft area and near-surface reflectivity area along with increasing near-surface cold pool area (Figs. 13-14), in agreement with the simulations of Grant and van den Heever (2014). Thus, for brevity, only the weak (ML25) and strong (ML50) mid-level shear simulations using strong low-level (LL20) and upper-level (UL25) shear with the drier (DRY), CTRL, or moister (MOIST) free tropospheric RH profile are described in further detail.

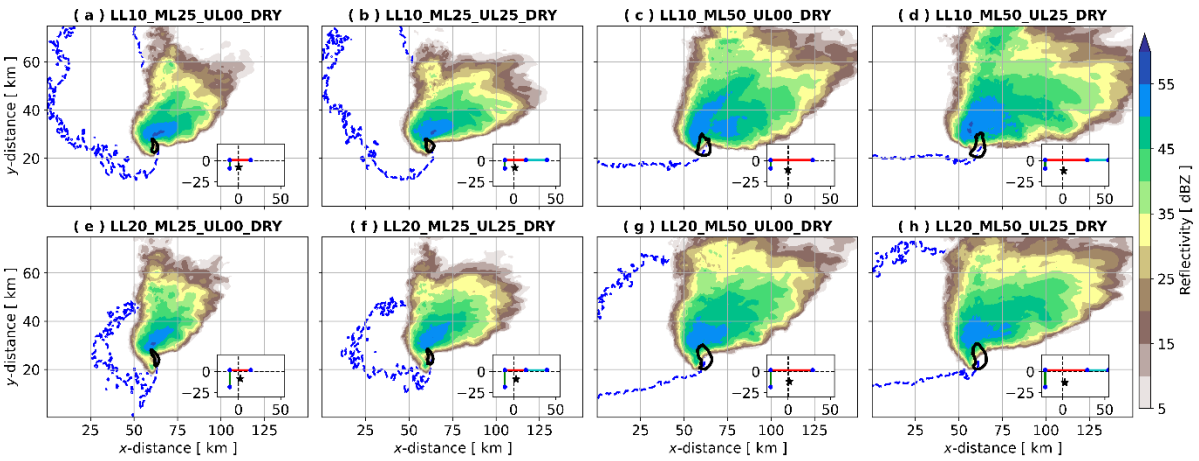

Fig. 13. As in Fig. 3, but for DRY simulations.

Accepted for publication in *Monthly Weather Review*. DOI 10.1175/MWR-D-23-0166.1.

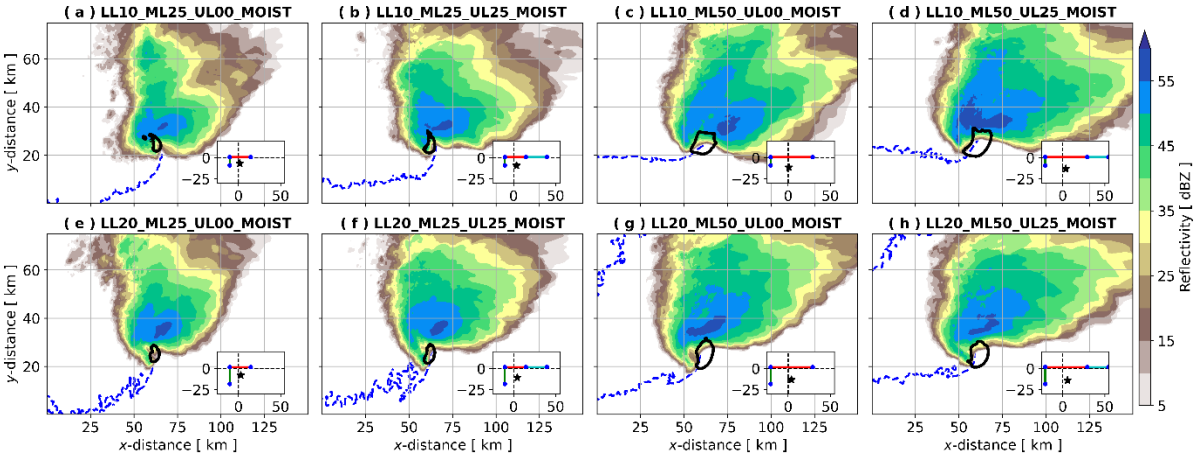

Fig. 14. As in Fig. 3, but for MOIST simulations.

Increasing mid-level shear and free tropospheric RH leads to increasing near-surface precipitation rate and area, along with surface precipitation accumulation (Figs. 15-16), supporting the larger near-surface cold pool area (Figs. 3 and 13-14). Percent differences between the ML25 and ML50 near-surface precipitation rates and precipitation accumulations are fairly consistent across the 90–180 min output timeframe and generally range between 20–60% (Fig. 16c,d). Time series of mid-level core updraft area and near-surface core reflectivity area confirm visual inspection of Figs. 13-14 in that as mid-level shear increases, mid-level updraft and near-surface reflectivity area become larger (Fig. 17). The same trend is also seen for higher free tropospheric RH (Fig. 17). Percent differences between the ML25 and ML50 maximum mid-level core updraft areas and near-surface core reflectivity areas across the 90–180 min output timeframe generally range between 20–70% (Fig. 17c,d). Core updraft area is also larger across the entire depth of the troposphere with stronger mid-level shear and higher free tropospheric RH (Fig. 18a), resulting in less dilute core updrafts with greater MSE between approximately 5–13 km than in the weaker mid-level shear and drier free tropospheric RH simulations (Fig. 18b). Percent differences between the ML25 and ML50 core updraft area and core updraft MSE composite vertical profiles generally range between 60–70% above the freezing level, or above ~3.5 km and between 0–5% across 5–13 km, respectively (Fig. 18e,f).

Accepted for publication in *Monthly Weather Review*. DOI 10.1175/MWR-D-23-0166.1.

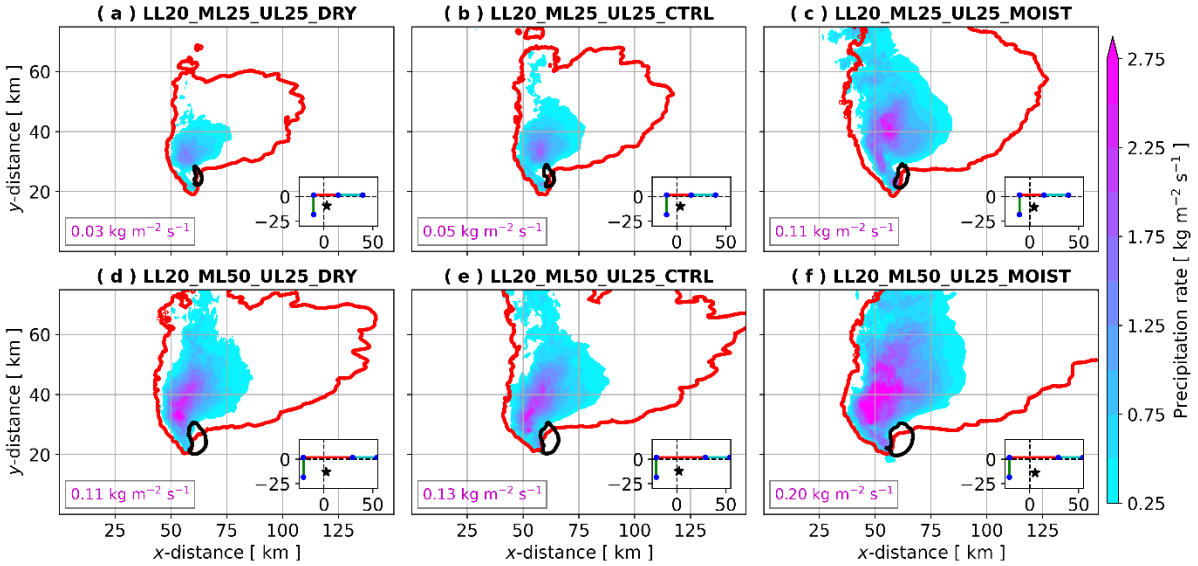

Fig. 15. As in Fig. 4 only for LL20 and UL25 vertical wind profiles with either ML25 (top row) and ML50 (bottom row) vertical wind profiles for DRY (left panels), CTRL (middle panels), and MOIST (right panels) simulations. Note the slightly different panel layout than Fig. 4.

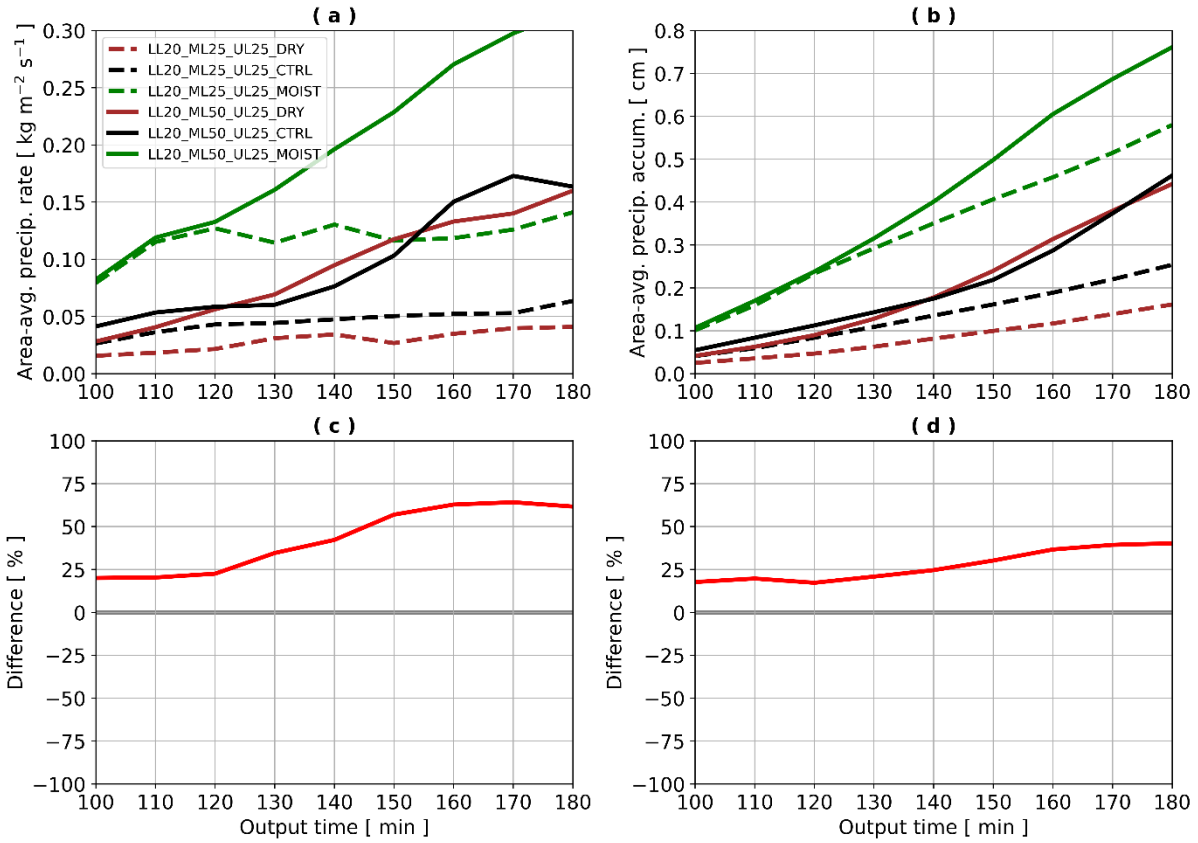

Fig. 16. As in Fig. 5 only for LL20 and UL25 vertical wind profiles with either ML25 (dashed lines) and ML50 (solid lines) vertical wind profiles for DRY (brown lines), CTRL (black lines), and MOIST (green lines) simulations.

Accepted for publication in *Monthly Weather Review*. DOI 10.1175/MWR-D-23-0166.1.

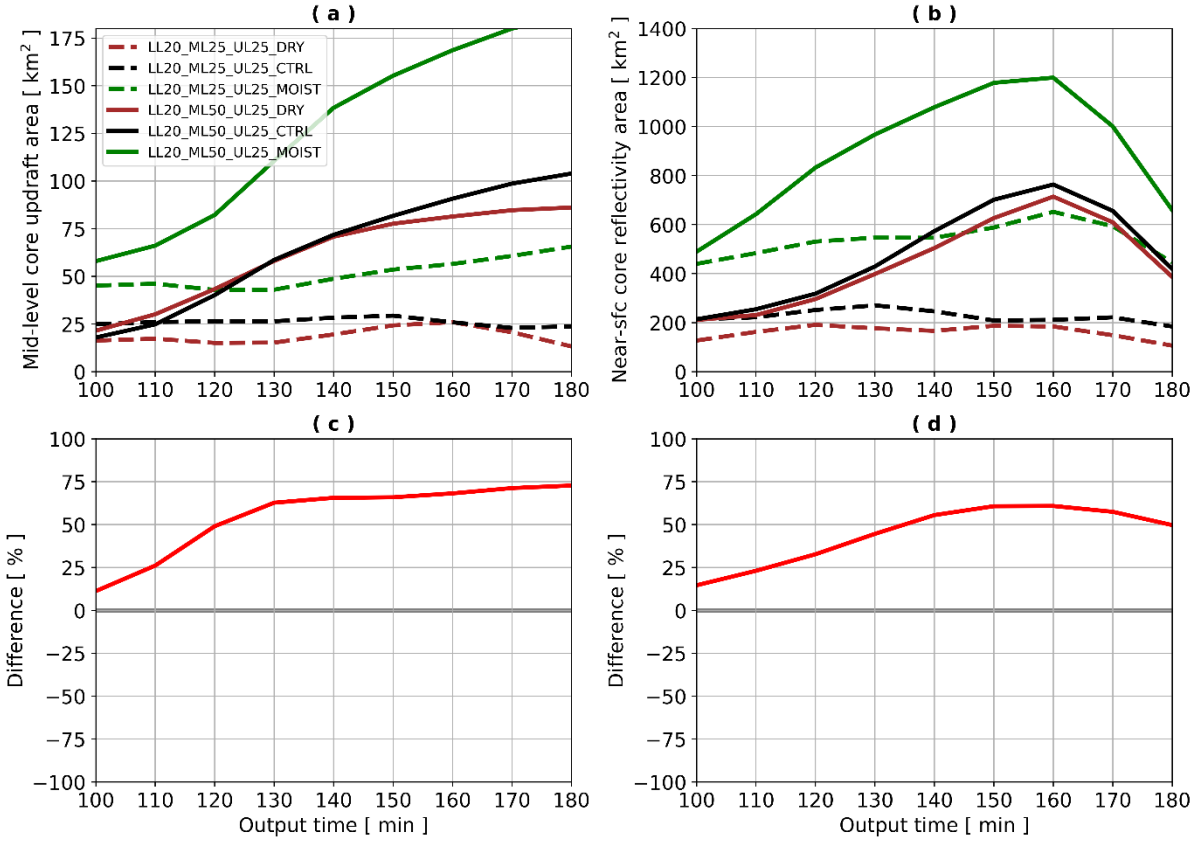

Fig. 17. As in Fig. 6 only for LL20 and UL25 vertical wind profiles with either ML25 (dashed lines) and ML50 (solid lines) vertical wind profiles for DRY (brown lines), CTRL (black lines), and MOIST (green lines) simulations.

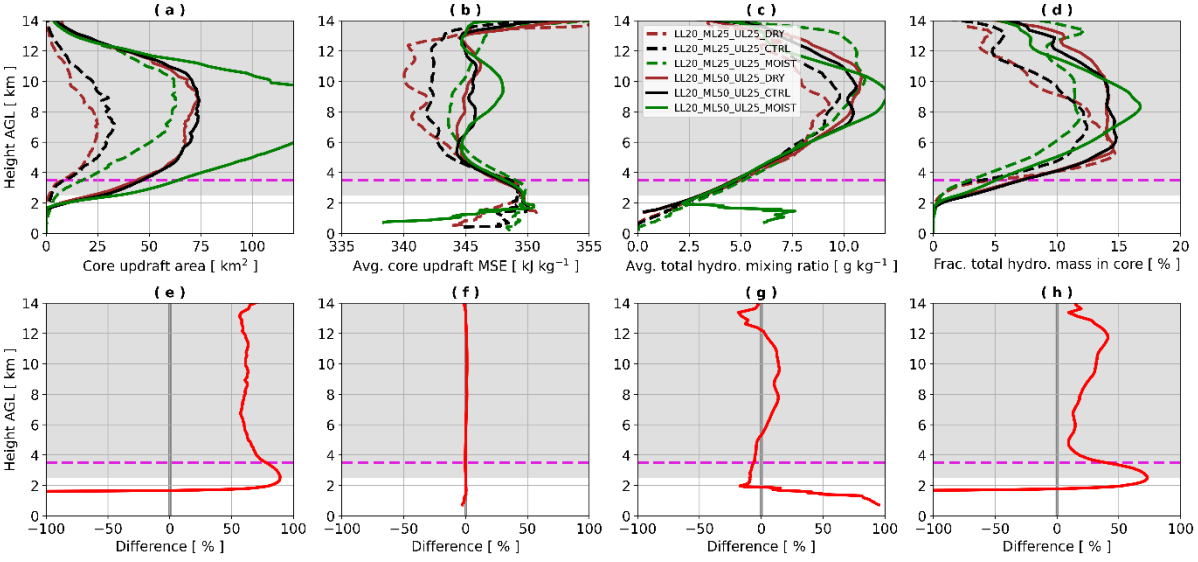

Fig. 18. As in Fig. 7 only for LL20 and UL25 vertical wind profiles with either ML25 (dashed lines) and ML50 (solid lines) vertical wind profiles for DRY (brown lines), CTRL (black lines), and MOIST (green lines) simulations. The gray shaded area in each panel denotes the layer over which the RH was altered above 2.5 km for the DRY and MOIST simulations.

Accepted for publication in *Monthly Weather Review*. DOI 10.1175/MWR-D-23-0166.1.

Composite vertical profiles of maximum updraft and downdraft strength reveal that, as in the CTRL simulations, stronger mid-level shear leads to stronger low-to-mid-level updrafts (Fig. 19a; right side) and stronger downdrafts throughout the entire troposphere (Fig. 19a; left side) in the DRY and MOIST simulations. Percent differences between the ML25 and ML50 simulations range up to 20% around the freezing level (~3.5 km) for updrafts (red solid line in Fig. 19d) and around 20–30% throughout the troposphere for downdrafts (red dashed line in Fig. 19d). This result supports the connection between updraft and downdraft strength as noted in previous observational (e.g., Lucas et al. 1994) and idealized numerical modeling (e.g. Marion and Trapp 2019) studies. Subtle variations exist, however, between the DRY, CTRL, and MOIST simulations. For example, mid-to-upper level downdrafts (above 6 km) in the ML50 simulations (solid lines in Fig. 19a; left side) are stronger (by ~5–10 m s^{-1}) in DRY simulations than MOIST simulations, but the opposite is true for ML25 simulations (dashed lines in Fig. 19a; left side) with differences also ~5–10 m s^{-1}. Stronger downdrafts in the DRY simulations agree with the results of Gilmore and Wicker (1998), whereas stronger downdrafts in the MOIST simulations agree with the results of James and Markowski (2010). Reasons for these downdraft differences based upon the mid-level shear magnitudes tested here are not clear and are beyond the scope of the current paper. Mid-to-upper-level updrafts (above 6 km) in the ML50 simulations (solid lines in Fig. 19a; right side) are stronger (~5–10 m s^{-1}) in the DRY simulations than the MOIST simulations (perhaps due to less hydrometeor loading in the DRY simulations, e.g., Fig. 18c), but the opposite is true for the ML25 simulations (dashed lines in Fig. 19a; right side) – perhaps due to greater buoyancy aloft owing to enhanced latent heat release (due to freezing) with the additional hydrometeor mass existing above the freezing level (Figs. 18c, 19b,c,h,i) – with differences of ~5 m s^{-1}. Lastly, low-to-mid-level (approximately 1–4 km) updrafts in the ML25 simulations (dashed lines in Fig. 19a; right side) are stronger (~5–10 m s^{-1}) in the MOIST simulations than the DRY or CTRL simulations possibly due to increased dynamic lift stemming from wider updrafts (e.g., Fig. 18a), and thus, stronger mesocyclones.

Accepted for publication in *Monthly Weather Review*. DOI 10.1175/MWR-D-23-0166.1.

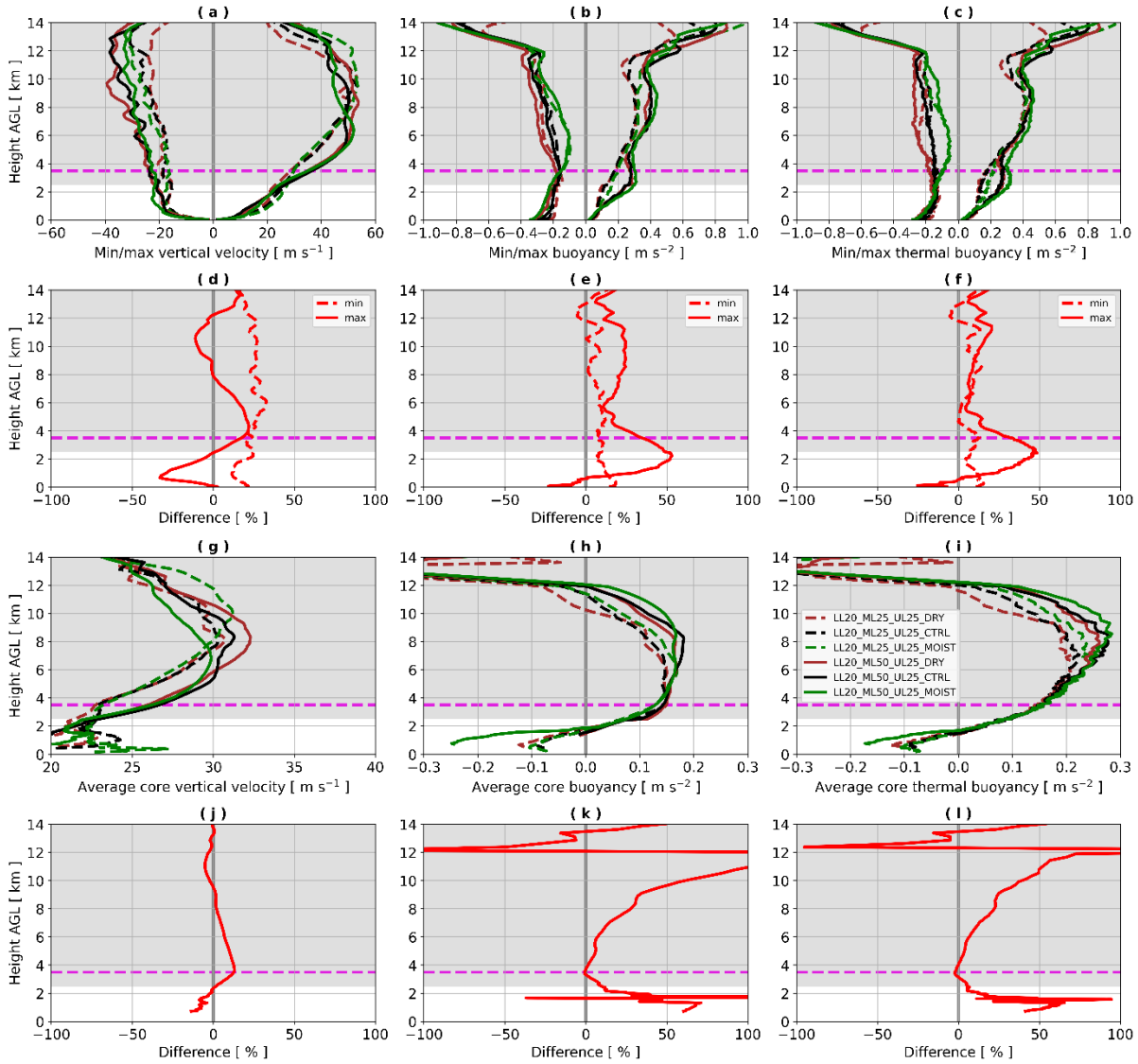

Fig. 19. As in Fig. 8 only for LL20 and UL25 vertical wind profiles with either ML25 (dashed lines) and ML50 (solid lines) vertical wind profiles for DRY (brown lines), CTRL (black lines), and MOIST (green lines) simulations. The gray shaded area in each panel denotes the layer over which the RH was altered above 2.5 km for the DRY and MOIST simulations.

Composite vertical profiles of average hydrometeor mass within core updrafts reveal, as in the CTRL simulations, that increasing mid-level shear yields greater hydrometeor loading within updrafts, especially between 5–12 km (Fig. 18c), owing to updrafts being wider (Figs. 17a,18a), less dilute (Fig. 18b), and thus stronger (Fig. 19a; right side). Percent differences between the ML25 and ML50 composite vertical profiles of average hydrometeor mass within core updrafts range between 0–15% between approximately 5–12 km (Fig. 18g). Hydrometeor loading is generally greater at mid-to-upper-levels within the MOIST simulations than the DRY simulations, which is especially evident in the ML25 simulations (dashed lines in Fig. 18c), similar to the simulations of Jo and Lasher-Trapp (2022). Furthermore, the fraction of hydrometeor mass existing within core updrafts relative to that within the entire right-moving

Accepted for publication in *Monthly Weather Review*. DOI 10.1175/MWR-D-23-0166.1.

supercell sub-domain is greater in the stronger mid-level shear simulations (i.e., ~12.5% for weaker mid-level shear compared to ~15% for stronger mid-level shear), especially between 5–12 km (Fig. 18d), and is also generally greater for the DRY simulations than the CTRL or MOIST simulations. Percent differences between the ML25 and ML50 hydrometeor mass existing within core updrafts relative to that within the entire right-moving supercell sub-domain composite vertical profiles range between 10–40% between approximately the freezing level (~3.5 km) and 12 km (Fig. 18h).

Greater hydrometeor mass within core updrafts amid stronger mid-level shear and higher RH does not lead to large reductions in updraft maxima (Fig. 19b; right side) or average core buoyancy (Fig. 19h), however. In fact, maximum updraft buoyancy is larger, especially across low- and upper-levels, in the stronger mid-level shear simulations (as seen prior in the CTRL simulations; Fig. 8b; red solid line in Fig. 19e), and maximum updraft buoyancy is also slightly larger in the higher RH simulations than the DRY or CTRL simulations (Fig. 19b). Percent differences between the ML25 and ML50 maximum buoyancy within core updrafts composite vertical profiles generally range between 10–50% and 10–25% over the 1–4 km and 6–12 km layers, respectively (red solid line in Fig. 19e). As in the CTRL simulations, the additional hydrometeor mass and loading within core updrafts amid stronger mid-level shear is compensated by greater maximum (Fig. 19c; right side) and average core (Fig. 19i) thermal buoyancy owing to wider (Figs. 17a, 18a), less dilute (Fig. 18b) core updrafts in stronger mid-level shear simulations. The same holds true with changes to the free tropospheric RH. Hydrometeor mass is greater outside of core updrafts in the stronger mid-level shear simulations (Fig. 20a), owing to the stronger storm-relative winds that horizontally displace more of the hydrometeor mass downshear of the updrafts in the DRY, CTRL, and MOIST simulations. Percent differences between the ML25 and ML50 hydrometeor mass outside of core updraft composite vertical profiles generally range between 40–50% across the depth of the troposphere (Fig. 20d). Hydrometeor mass outside of core updrafts increases as free tropospheric RH increases for both the ML25 (dashed lines in Fig. 20a) and ML50 (solid lines in Fig. 20a) simulations given that there is more hydrometer mass within core updrafts that detrains in these higher free tropospheric RH environments (Fig. 18c).

Accepted for publication in *Monthly Weather Review*. DOI 10.1175/MWR-D-23-0166.1.

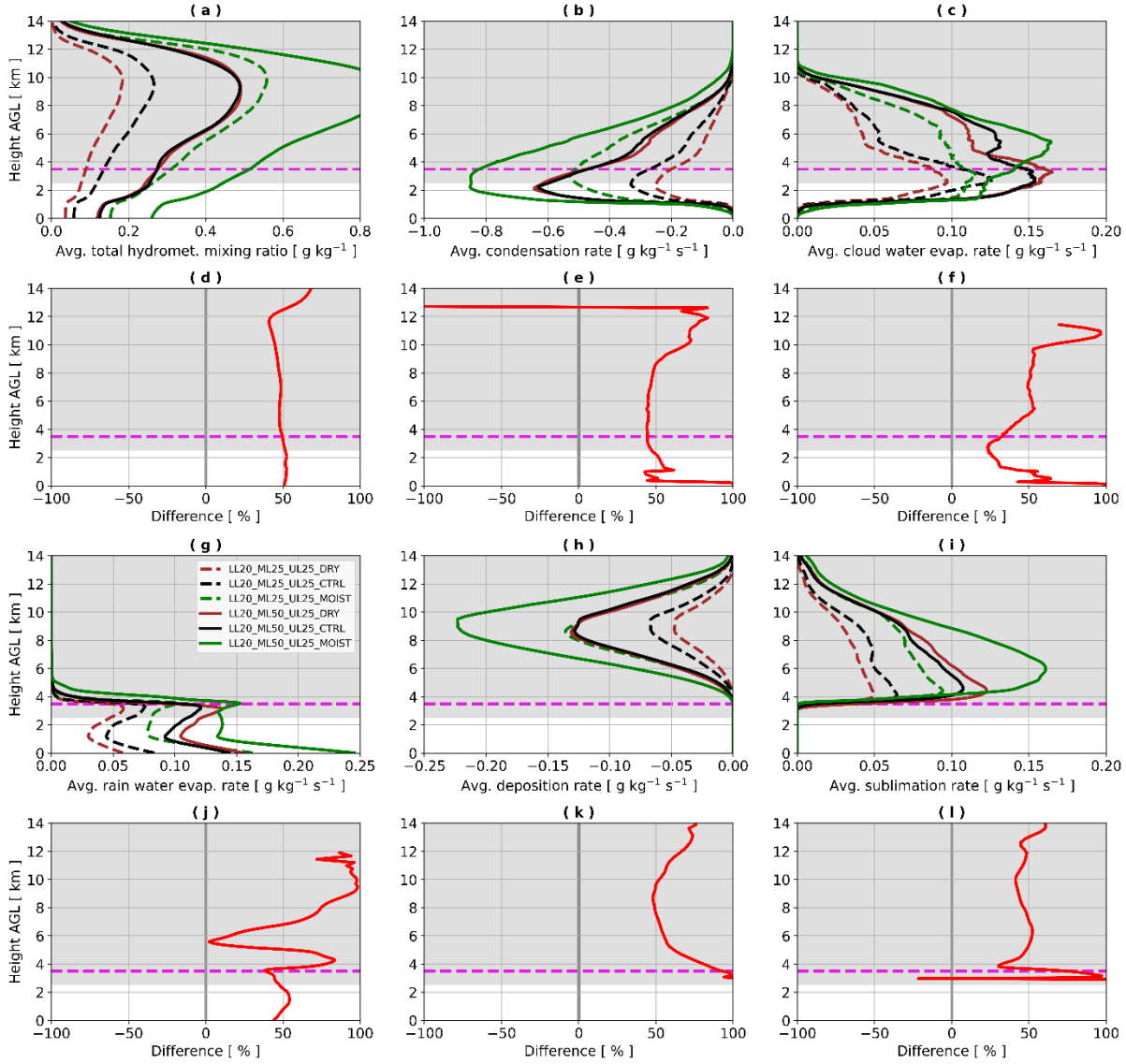

Fig. 20. As in Fig. 9 only for LL20 and UL25 vertical wind profiles with either ML25 (dashed lines) and ML50 (solid lines) vertical wind profiles for DRY (brown lines), CTRL (black lines), and MOIST (green lines) simulations. The gray shaded area in each panel denotes the layer over which the RH was altered above 2.5 km for the DRY and MOIST simulations.

As previously shown for the CTRL simulations, plan view and west-to-east oriented vertical cross section composites of a selection of water vapor budget terms (Figs. 21-22) show that rates of both sublimation at mid-to-upper levels and evaporation at lower levels increase with increasing mid-level shear. These regions of sublimation and evaporation are larger and more horizontally extensive downshear within stronger mid-level shear environments (Figs. 21-22; compare top row and bottom row). Spatially, there are only subtle variations in these water vapor budget terms due to changes in free tropospheric RH (Figs. 21-22; compare all three panels across either the top row or bottom row). However, all terms in the water vapor budget are larger in stronger mid-level shear and higher free tropospheric RH simulations (Fig.

Accepted for publication in *Monthly Weather Review*. DOI 10.1175/MWR-D-23-0166.1.

20b-c and g-i) with percent differences between the ML25 and ML50 simulations of generally between 20–70% (Fig. 20e-f and j-l). Generally, the MOIST simulations exhibit greater cloud (Fig. 20c) and rain water (Fig. 20g) evaporation, along with sublimation (Fig. 20i), than the DRY simulations, given that more hydrometeor mass is located outside of core updrafts in a moister free tropospheric environment (Fig. 20a). Thus, even though one might anticipate lower sublimation and evaporation rates in a moister environment than a drier environment with all else being equal, this is compensated by more hydrometeor mass being available to sublimate or evaporate in the moister environment.

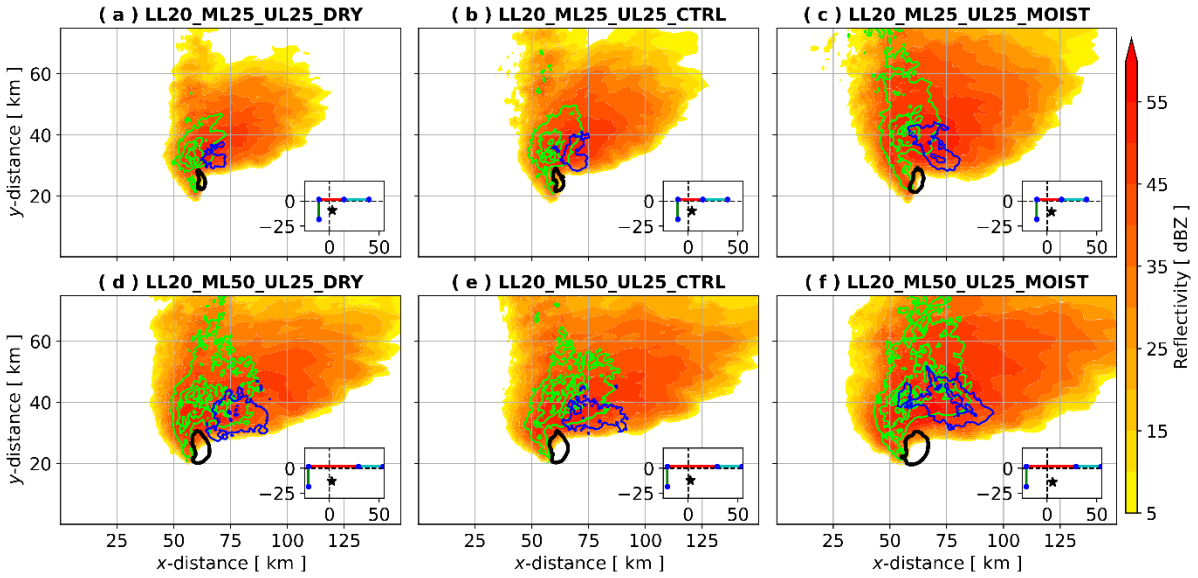

Fig. 21. As in Fig. 11 only for LL20 and UL25 vertical wind profiles with either ML25 (top row) and ML50 (bottom row) vertical wind profiles for DRY (left panels), CTRL (middle panels), and MOIST (right panels) simulations. Note the slightly different panel layout than Fig. 11.

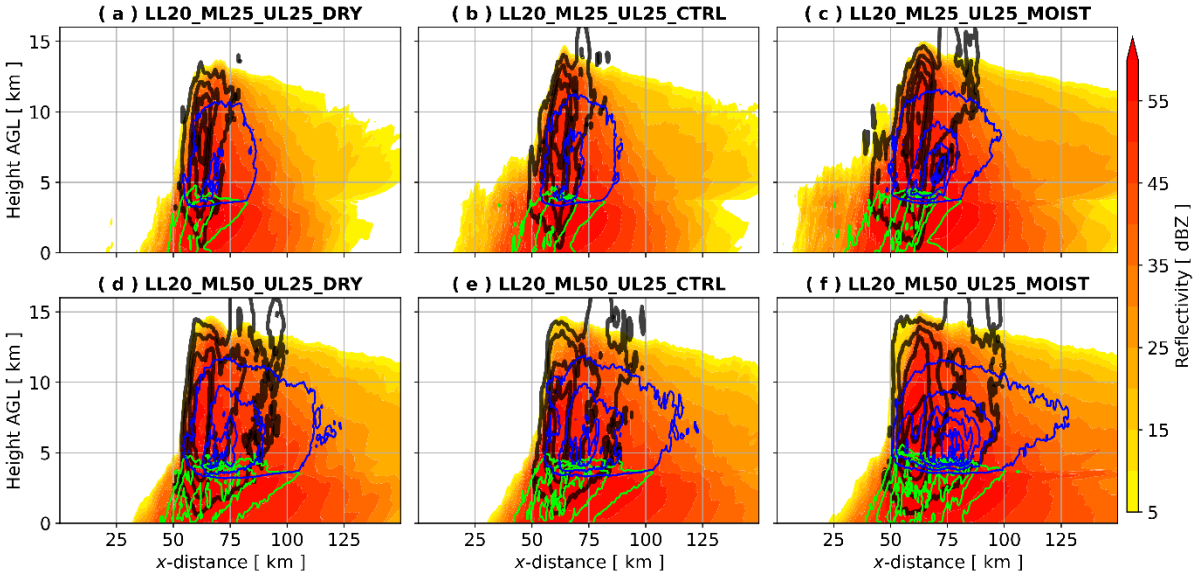

Accepted for publication in *Monthly Weather Review*. DOI 10.1175/MWR-D-23-0166.1.

Fig. 22. As in Fig. 12 only for LL20 and UL25 vertical wind profiles with either ML25 (top row) and ML50 (bottom row) vertical wind profiles for DRY (left panels), CTRL (middle panels), and MOIST (right panels) simulations. Note the slightly different panel layout than Fig. 12.

4. Summary and conclusions

This study explores the relationship between shear magnitude, updraft area, and precipitation area within simulated supercell thunderstorms to determine how changes in shear magnitude across different vertical layers (lower, middle, or upper troposphere) and free tropospheric RH impact updraft characteristics and hydrometeor distributions. It has long been known that shear impacts supercells by horizontally displacing hydrometeor mass (and resultant downdrafts) downshear of the updraft owing to strong storm-relative winds aloft. However, updraft size and strength also scales with shear magnitude, which may potentially result in a more expansive horizontal region over which hydrometeor mass develops and lead to greater hydrometeor loading within updrafts.

To address the uncertainties related to the effects of shear on hydrometeor distributions in supercells, and to determine how changes in shear across different layers impacts these hydrometeor distributions, a suite of idealized model simulations of supercells were conducted. Shear was systematically altered across different layers to produce a range of supercell sizes and strengths in a fixed thermodynamic environment. Furthermore, the results from these initial control simulations are compared to those in drier and moister free tropospheric environments to evaluate if the trends with changes to shear were agnostic to the environmental free tropospheric relative humidity. These simulations also clarify the role of environmental free tropospheric relative humidity on hydrometeor distributions in supercells.

The main findings from analysis of the control simulations (with the unaltered thermodynamic sounding) are that stronger shear, especially across mid-levels (in this case, 1–6 km), leads to stronger storm-relative inflow and thus, wider, less dilute, and stronger updrafts. Furthermore, stronger mid-level shear leads to greater precipitation rates and accumulation over a larger area, a larger region of near-surface reflectivity, and a more expansive near-surface cold pool. Both hydrometeor mass and the relative fraction of hydrometeor mass within core updrafts compared to the total hydrometeor mass within the entire right-moving supercell sub-domain were greater amid strong mid-level shear. However, the wider, less dilute updrafts in these stronger mid-level shear simulations exhibit larger thermal buoyancy, which compensates for the additional hydrometeor loading, and results in greater total buoyancy

Accepted for publication in *Monthly Weather Review*. DOI 10.1175/MWR-D-23-0166.1.

overall. Although representing a slightly smaller fraction of the hydrometeors produced, more total hydrometeor mass is transported farther downshear in stronger mid-level shear simulations.

This additional hydrometeor mass displaced away from updrafts leads to greater rates of sublimation at mid-to-upper levels and evaporation at low-levels in stronger mid-level shear simulations. This may also help to explain stronger downdrafts throughout the troposphere in stronger mid-level shear simulations, in addition to increased hydrometeor loading outside of core updrafts. The direction of the mid-to-upper-level (i.e., above 5 km) storm-relative winds appears most determinative of where the near-surface precipitation/reflectivity core is located relative to the main updraft. This study, which reveals that 1–6 km shear magnitudes appear most determinative of pertinent supercell properties (e.g., updraft width, hydrometeor concentrations, etc.), lends credence to previous studies that have predominantly analyzed sensitivity of a variety of supercell properties to mid-level (typically 3–6 km) shear variations in idealized simulations and to supercell forecast parameters that typically leverage 0–6 km shear. While the main goal of this study was not to refute the hypothesis that 0–6 km shear is just as, if not more important, than 1–6 km shear for determining the relationships shown here, a recent study by Nixon and Allen (2022) showed that the difference in skill between 0–6 km and 1–6 km shear magnitudes in predicting large hail and/or tornado occurrence from supercells was minimal (Figs. 4 and 5 therein). Additional simulations are needed to better determine if the 0–6 or 1–6 km shear is most relevant for the specific proposed mechanisms shown here.

Finally, these results are consistent across the free tropospheric relative humidity sensitivity simulations. The supercells in moister free tropospheric environments additionally exhibited wider updraft cores, greater hydrometeor mass both within and outside core updrafts, and perhaps surprisingly, greater sublimation and evaporation rates owing to more hydrometeor mass existing outside of core updrafts in higher free tropospheric relative humidity environments.

Future work is needed to further test the robustness of the results presented here. Intensive observational studies are needed to confirm these idealized modeling results. For example, supercell updraft and precipitation area size can be estimated from radar-derived products, such as differential reflectivity columns and near-surface reflectivity, respectively.

Accepted for publication in *Monthly Weather Review*. DOI 10.1175/MWR-D-23-0166.1.

These observed storm properties can then be related to environmental variables, such as shear across various layers and free tropospheric relative humidity, via analysis of near-storm observed and/or model soundings. Furthermore, additional simulations utilizing different magnitudes or layers of CAPE, CIN, EIL depths, and shear, among other variables, along with varying planetary boundary layer relative humidity, for example, are needed. Future work should explore the sensitivities of how shear is vertically distributed across various atmospheric layers (more than the three we used here) to test the robustness of the mechanisms discussed herein. Furthermore, understanding how these results change for supercells traversing time-varying vertical wind and/or thermodynamic environments, such as leveraging the base-state substitution (BSS) method in CM1 (e.g., Letkewicz et al. 2013; Coffer and Parker 2015; Davenport et al. 2019), would additionally be beneficial. The work presented here is the first step in ongoing research analyzing the dominant mechanisms for downdraft formation (i.e., evaporative cooling, hydrometeor loading, perturbation pressure gradient accelerations) within supercell thunderstorms.

Acknowledgments.

The authors would like to thank the following people for constructive feedback and fruitful discussion throughout the entirety of this multi-year project: Drs. Matthew Kumjian (Pennsylvania State University), Marcus Van Lier-Walqui (Columbia University), Scott Steiger (State University of New York at Oswego), Bruce Lee (University of North Dakota), and Bowen Pan (Colorado State University; RTI International). Furthermore, the authors would like to thank the tremendous and highly detailed reviews from the three anonymous reviewers along with the Main Editor, Dr. Zhiyong Meng, which greatly improved the quality and presentation of this work. Helpful feedback was also provided by Johana Lambert and Janice Mulholland. J. Mulholland personally thanks G. Marion (National Severe Storms Laboratory) for sharing the initial version of the updraft area code that he developed. J. Mulholland, J. Peters, and H. Morrison were supported by DOE Grant DE-SC0022942. C. Nowotarski and E. Nielsen were supported by NSF Grant AGS-2149354. The idealized numerical model simulations were run on the NCAR Derecho Supercomputer (https://doi.org/10.5065/qx9a-pg09), and thus, we would like to acknowledge high-performance computing support from NCAR's Computational and Information Systems

Laboratory, which is sponsored by NSF. Finally, this paper is dedicated to J. Mulholland's newborn daughter, Amelia.

Data Availability Statement.

All model namelist files, input soundings, Python analysis scripts, etc., have been uploaded for open access to the following URL: https://figshare.com/projects/How_does_vertical_wind_shear_influence_updraft_characteristics_and_hydrometeor_characteristics_distributions_in_supercell_thunderstorms_/173937. For any additional questions, please contact the corresponding author via email.

APPENDIX A

Additional sensitivity test #1: Altering the microphysics parameterization scheme

As described in section 2j, the first of two additional sensitivity tests that was performed involved changing the microphysics parameterization scheme from the Morrison two-moment (MORR) scheme to the NSSL two-moment scheme, which, unlike the MORR scheme, includes the concurrent representation of both graupel and hail ice species. Analysis of the plan view composites reveal that even though structural differences exist between the MORR and NSSL simulations, especially in terms of their near-surface reflectivity and near-surface cold pool patterns (e.g., NSSL simulations exhibit larger near-surface reflectivity magnitudes, but over a smaller area than MORR simulations; NSSL simulations exhibit smaller near-surface cold pool areas than MORR simulations), the results presented in section 3 remain consistent for both microphysics parameterization schemes (Figs. S3-S4). In other words, as shear increases, especially mid-level shear, mid-level updraft area, near-surface reflectivity area, and near-surface cold pool area all increase (Figs. S3-S4; compare top row with bottom row). Furthermore, composite vertical profiles are generally consistent between the MORR and NSSL simulations, showing that the amount of hydrometeor mass both inside and outside core updrafts increase as mid-level shear and free tropospheric RH increase (Fig. S5a,b,d,e). The biggest difference in the composite vertical profiles between the MORR and NSSL simulations is that the MORR DRY simulations exhibit the largest relative fraction of hydrometeor mass inside core updrafts (Fig. S5c). Alternatively, the NSSL MOIST simulations with ML50 exhibit the largest relative fraction of hydrometeor mass within core updrafts between approximately

File generated with AMS Word template 2.0

Accepted for publication in *Monthly Weather Review*. DOI 10.1175/MWR-D-23-0166.1.

5–10 km (i.e., ~17.5% for the NSSL DRY or CTRL simulations compared to ~20% for the NSSL MOIST simulations; solid lines in Fig. S5f), which aligns with the region of greater hydrometeor mass inside core updrafts between these levels in the MOIST simulations with ML50 (solid lines in Fig. S5d). Only relatively minor differences exist in the largest relative fraction of hydrometeor mass within core updrafts in the NSSL simulations between DRY, CTRL, and MOIST with ML25 (dashed lines in Fig. S5f). Finally, percent differences (please see section 2i) between the ML25 and ML50 simulations for the composite vertical profiles shown in Fig. S5 display similar patterns and magnitudes between the MORR and NSSL simulations (Fig. S6; top two rows).

APPENDIX B

Additional sensitivity test #2: Altering the specified cloud droplet number concentration

As described in section 2j, the second of two additional sensitivity tests that was performed involved changing the specified cloud droplet number concentration in the Morrison two-moment scheme from the default concentration of 250 cm^{-3} to either a low, pristine, maritime concentration (50 cm^{-3}) or high, polluted, continental concentration (1000 cm^{-3}) to alter the amount of hydrometeor loading within the simulations. Plan view composites between the 50 cm^{-3} (Fig. S7), 250 cm^{-3} (Fig. S3), and 1000 cm^{-3} (Fig. S8) simulations reveal only relatively minor differences (i.e., much smaller than the differences noted between the MORR and NSSL simulations). Similarly, composite vertical profiles reveal only relatively minor differences between the cloud droplet number concentration simulations and are consistent with the control (250 cm^{-3}) simulations (Fig. S5a-b) in that the amount of hydrometeor mass both inside and outside core updrafts increases as mid-level shear and free tropospheric RH increases (Fig. S5g,h,j,k), along with the greater relative fraction of hydrometeor mass within core updrafts in the DRY than in the CTRL or MOIST simulations (Fig. S5c,i,l). Finally, percent differences (please see section 2i) between the ML25 and ML50 simulations for the composite vertical profiles shown in Fig. S5 display similar patterns and magnitudes between the 50 cm^{-3}, MORR (250 cm^{-3}), and 1000 cm^{-3} simulations (Fig. S6; first row and bottom two rows).

REFERENCES

Accepted for publication in *Monthly Weather Review*. DOI 10.1175/MWR-D-23-0166.1.

Adlerman, E. J., K. K. Droegemeier, and R. Davies-Jones, 1999: A numerical simulation of cyclic mesocyclogenesis. *J. Atmos. Sci.*, **56**, 2045–2069.

Beatty, K., E. N. Rasmussen, and J. M. Straka, 2008: The supercell spectrum. Part I: A review of research related to supercell precipitation morphology. *Electron. J. Severe Storms Meteor.*, **3** (4), 1–21. [Available online at http://www.ejssm.org/ojs/index.php/ejssm/article/viewarticle/44/45.]

Beck, J., and C. Weiss, 2013: An assessment of low-level baroclinity and vorticity within a simulated supercell. *Mon. Wea. Rev.*, **141**, 649–669.

Blumberg, W. G., K. T. Halbert, T. A. Supinie, P. T. Marsh, R. L. Thompson, and J. A. Hart, 2017: SHARPpy: An open-source sounding analysis toolkit for the atmospheric sciences. *Bull. Amer. Meteor. Soc.*, **98**, 1625–1636, https://doi.org/10.1175/BAMS-D-15-00309.1.

Brooks, H. E., C. A. Doswell, and J. Cooper, 1994a: On the environments of tornadic and nontornadic mesocyclones. *Wea. Forecasting*, **9**, 606–618.

Brooks, H. E., C. A. Doswell III, and R. B. Wilhelmson, 1994b: The role of midtropospheric winds in the evolution and maintenance of low-level mesocyclones. *Mon. Wea. Rev.*, **122**, 126–136.

Browning, K., 1977: The structure and mechanism of hailstorms. *Hail: A Review of Hail Science and Hail Suppression, Meteor. Monogr.*, No. 38, Amer. Meteor. Soc., 1–43.

Bryan, G. H., and J. M. Fritsch, 2002: A benchmark simulation for moist nonhydrostatic numerical models. *Mon. Wea. Rev.*, **130**, 2917–2928.

Chavas, D. R., and D. T. Dawson II, 2021: An idealized physical model for the severe convective storm environmental sounding. *J. Atmos. Sci.*, **78**, 653–670.

Accepted for publication in *Monthly Weather Review*. DOI 10.1175/MWR-D-23-0166.1.

Coffer, B. E., and M. D. Parker, 2015: Impacts of increasing low-level shear on supercells during the early evening transition. *Mon. Wea. Rev.*, **143**, 1945–1969.

Davenport, C. E., C. L. Ziegler, and M. I. Biggerstaff, 2019: Creating a more realistic idealized supercell thunderstorm evolution via incorporation of base-state environmental variability. *Mon. Wea. Rev.*, **147**, 4177–4198, https://doi.org/10.1175/MWR-D-18-0447.1.

Davies-Jones, R. P., 1982: Observational and theoretical aspects of tornado-genesis. *Intense Atmospheric Vortices*, L. Bengtsson and J. Lighthill, Eds., Springer-Verlag, 175–189.

Davies-Jones, R. P., and H. E. Brooks, 1993: Mesocyclogenesis from a theoretical perspective. *The Tornado: Its Structure, Dynamics, Prediction, and Hazards*, Geophys. Monogr., No. 79, Amer. Geophys. Union, 105–114.

Deardorff, J. W., 1980: Stratocumulus-capped mixed layers derived from a three-dimensional model. *Bound.-Layer Meteor.*, **18**, 495–527.

Dennis, E. J., and M. R. Kumjian, 2017: The impact of vertical wind shear on hail growth in simulated supercells. *J. Atmos. Sci.*, **74**, 641–663.

Duda, J. D., and W. A. Gallus Jr., 2010: Spring and summer Mid-western severe weather reports in supercells compared to other morphologies. *Wea. Forecasting*, **25**, 190–206.

Durran, D. R., and J. B. Klemp, 1983: A compressible model for the simulation of moist mountain waves. *Mon. Wea. Rev.*, **111**, 2341–2361.

Emanuel, K. A., 1994: *Atmospheric Convection*. Oxford University Press, 588 pp.

Finley, C. A., W. R. Cotton, and R. A. Pielke Sr., 2001: Numerical simulation of tornadogenesis in a high-precipitation supercell. Part I: Storm evolution and transition into a bow echo. *J. Atmos. Sci.*, **58**, 1597–1629.

Accepted for publication in *Monthly Weather Review*. DOI 10.1175/MWR-D-23-0166.1.

Finley, C. A., M. Elmore, L. Orf, and B. D. Lee, 2023: Impact of the streamwise vorticity current on low-level mesocyclone development in a simulated supercell. *Geophys. Res. Lett.*, **50**, e2022GL100005.

Foote, G., and J. Fankhauser, 1973: Airflow and moisture budget beneath a northeast Colorado hailstorm. *J. Appl. Meteor. Climatol.*, **12**, 1330–1353.

Frame, J. W., and P. M. Markowski, 2010: Numerical simulations of radiative cooling beneath the anvils of supercell thunder-storms. *Mon. Wea. Rev.*, **138**, 3024–3047.

Frame, J. W., and P. M. Markowski, 2013: Dynamical influences of anvil shading on simulated supercell thunderstorms. *Mon. Wea. Rev.*, **141**, 2802–2820.

Frame, J., and G. Nelson, 2022: Distinguishing between high-precipitation and low-precipitation supercell environments. *30th Conf. on Severe Local Storms*, Santa Fe, NM, Amer. Meteor. Soc., 67, https://ams.confex.com/ams/30SLS/meetingapp.cgi/Paper/407315.

French, M. M., and D. M. Kingfield, 2021: Tornado formation and intensity prediction using polarimetric radar estimates of updraft area. *Wea. Forecasting*, **36**, 2211–2231.

Gilmore, M. S., and L. J. Wicker, 1998: The influence of mid-tropospheric dryness on supercell morphology and evolution. *Mon. Wea. Rev.*, **126**, 943–958.

Grant, L. D., and S. C. van den Heever, 2014: Microphysical and dynamical characteristics of low-precipitation and classic supercells. *J. Atmos. Sci.*, **71**, 2604–2624.

Gray, K., and J. Frame, 2021: The impact of midlevel shear orientation on the longevity of and downdraft location and tornado-like vortex formation within simulated super-cells. *Mon. Wea. Rev.*, **149**, 3739–3759.

Hitchens, N. M., and H. E. Brooks, 2013: Preliminary investigation of the contribution of supercell thunderstorms to the climatology of heavy and extreme precipitation in the United States. *Atmos. Res.*, **123**, 206–210.

Accepted for publication in *Monthly Weather Review*. DOI 10.1175/MWR-D-23-0166.1.

James, R. P., and P. M. Markowski, 2010: A numerical investigation of the effects of dry air aloft on deep convection. *Mon. Wea. Rev.*, **138**, 140–161.

Jo, E., and S. Lasher-Trapp, 2022: Entrainment in a simulated supercell thunderstorm. Part II: The influence of vertical wind shear and general effects upon precipitation. *J. Atmos. Sci.*, **79**, 1429–1443.

Jo, E., and S. Lasher-Trapp, 2023: Entrainment in a simulated supercell thunderstorm. Part III: The influence of decreased environmental humidity and general effects upon precipitation. *J. Atmos. Sci.*, **80**, 1107–1122.

Kiefer, P. J., 1941: The thermodynamic properties of water and water vapor. *Mon. Wea. Rev.*, **69**, 329–332.

Klemp, J. B., and R. Rotunno, 1983: A study of the tornadic region within a supercell thunderstorm. *J. Atmos. Sci.*, **40**, 359–377.

Kreitzberg, C. W., 1964: The structure of occlusions as determined from serial ascents of vertically-directed radar. Air Force Cambridge Research Laboratory Rep. AFCRL-64-26, 121 pp.

Lee, B. D., C. A. Finley, and C. D. Karstens, 2012: The Bowdle, South Dakota, cyclic tornadic supercell of 22 May 2010: Surface analysis of rear-flank downdraft evolution and multiple internal surges. *Mon. Wea. Rev.*, **140**, 3419–3441.

Letkewicz, C. E., A. J. French, and M. D. Parker, 2013: Base-state substitution: An idealized modeling technique for approximating environmental variability. *Mon. Wea. Rev.*, **141**, 3062–3086, https://doi.org/10.1175/MWR-D-12-00200.1.

Loeffler, S. D., and M. R. Kumjian, 2018: Quantifying the separation of enhanced ZDR and KDP regions in nonsupercell tornadic storms. *Wea. Forecasting*, **33**, 1143–1157.

Loeffler, S. D., M. R. Kumjian, M. Jurewicz, and M. M. French, 2020: Differentiating between tornadic and nontornadic supercells using polarimetric radar signatures of hydrometeor size sorting. *Geophys. Res. Lett.*, **47**, e2020GL088242.

Accepted for publication in *Monthly Weather Review*. DOI 10.1175/MWR-D-23-0166.1.

Lucas, C., E. J. Zipser, and M. A. LeMone, 1994: Vertical velocity in oceanic convection off tropical Australia. *J. Atmos. Sci.*, **51**, 3183–3193.

Mansell, E. R., and C. L. Ziegler, 2013: Aerosol effects on simulated storm electrification and precipitation in a two-moment bulk microphysics model. *J. Atmos. Sci.*, **70**, 2032–2050.

Mansell, E. R., C. L. Ziegler, and E. C. Bruning, 2010: Simulated electrification of a small thunderstorm with two-moment bulk microphysics. *J. Atmos. Sci.*, **67**, 171–194.

Marion, G. R., and R. J. Trapp, 2019: The dynamical coupling of convective updrafts, downdrafts, and cold pools in simulated supercell thunderstorms. *J. Geophys. Res. Atmos.*, **124**, 664–683.

Markowski, P. M., C. Hannon, J. Frame, E. Lancaster, A. Pietrycha, R. Edwards, and R. L. Thompson, 2003: Characteristics of vertical wind profiles near supercells obtained from the Rapid Update Cycle. *Wea. Forecasting*, **18**, 1262–1272.

Markowski, P., and Y. Richardson, 2010: *Mesoscale Meteorology in Midlatitudes*. Wiley-Blackwell, 430 pp.

Markowski, P. M., and Y. Richardson, 2014: The influence of environmental low-level shear and cold pools on tornadogenesis: Insights from idealized simulations. *J. Atmos. Sci.*, **71**, 243–275.

Markowski, P., and Coauthors, 2012: The pretornadic phase of the Goshen County, Wyoming, supercell of 5 June 2009 intercepted by VORTEX2. Part II: Intensification of low-level rotation. *Mon. Wea. Rev.*, **140**, 2916–2938.

Marwitz, J. D., 1972: Precipitation efficiency of thunderstorms on the High Plains. *J. Rech. Atmos.*, **6**, 367–370.

Mashiko, W., H. Niino, and T. Kato, 2009: Numerical simulation of tornadogenesis in an outer-rainband minisupercell of Typhoon Shanshan on 17 September 2006. *Mon. Wea. Rev.*, **137**, 4238–4260.

McCaul, E. W., Jr., and M. L. Weisman, 1996: Simulations of shallow supercell storms in landfalling hurricane environments. *Mon. Wea. Rev.*, **124**, 408–429.

Accepted for publication in *Monthly Weather Review*. DOI 10.1175/MWR-D-23-0166.1.

Morrison, H., G. Thompson, and V. Tatarskii, 2009: Impact of cloud microphysics on the development of trailing stratiform precipitation in a simulated squall line: Comparison of one- and two-moment schemes. *Mon. Wea. Rev.*, **137**, 991–1007.

Mulholland, J. P., S. W. Nesbitt, R. J. Trapp, and J. M. Peters, 2020: The influence of terrain on the convective environment and associated convective morphology from an idealized modeling perspective. *J. Atmos. Sci.*, **77**, 3929–3949.

Nielsen, E. R., and R. S. Schumacher, 2018: Dynamical insights into extreme short-term precipitation associated with supercells and mesovortices. *J. Atmos. Sci.*, **75**, 2983–3009.

Nielsen, E. R., and R. S. Schumacher, 2020: Dynamical mechanisms supporting extreme rainfall accumulations in the Houston "Tax Day" Flood. *Mon. Wea. Rev.*, **148**, 83–109.

Nixon, C. J., J. T. Allen, and M. Taszarek, 2023: Hodographs and skew Ts of hail-producing storms. *Wea. Forecasting*, **38**, 2217–2236.

Nowotarski, C. J., and P. M. Markowski, 2016: Modifications to the near-storm environment induced by simulated supercell thunderstorms. *Mon. Wea. Rev.*, **144**, 273–293.

Orf, L., R. Wilhelmson, B. Lee, C. Finley, and A. Houston, 2017: Evolution of a long-track violent tornado within a simulated supercell. *Bull. Amer. Meteor. Soc.*, **98**, 45–68.

Parker, M. D., 2014: Composite VORTEX2 supercell environments from near-storm soundings. *Mon. Wea. Rev.*, **142**, 508–529.

Parker, M. D., 2017: How much does ''backing aloft'' actually impact a supercell? *Wea. Forecasting*, **32**, 1937–1957.

Peters, J. M., B. E. Coffer, M. D. Parker, C. J. Nowotarski, J. P. Mulholland, C. J. Nixon, and J. T. Allen, 2022d: Disentangling the influences of storm-relative flow and horizontal streamwise vorticity on low-level mesocyclones in supercells. *J. Atmos. Sci.*, **80**, 129–149.

Peters, J. M., C. J. Nowotarski, and H. Morrison, 2019: The role of vertical wind shear in modulating maximum supercell updraft velocities. *J. Atmos. Sci.*, **76**, 3169–3189.

Accepted for publication in *Monthly Weather Review*. DOI 10.1175/MWR-D-23-0166.1.

Peters, J. M., C. J. Nowotarski, J. P. Mulholland, and R. L. Thompson, 2020b: The influences of effective inflow layer streamwise vorticity and storm-relative flow on supercell updraft properties. *J. Atmos. Sci.*, **77**, 3033–3057.

Peters, J. M., and D. R. Chavas, 2021: Evaluating the conservation of energy variables in simulations of deep moist convection. *J. Atmos. Sci.*, **78**, 3229–3246.

Peters, J. M., H. Morrison, C. J. Nowotarski, J. P. Mulholland, and R. L. Thompson, 2020a: A formula for the maximum vertical velocity in supercell updrafts. *J. Atmos. Sci.*, **77**, 3747–3757.

Peters, J. M., H. Morrison, T. C. Nelson, J. N. Marquis, J. P. Mulholland, and C. J. Nowotarski, 2022b: The influence of shear on deep convection initiation. Part I: Theory. *J. Atmos. Sci.*, **79**, 1669–1690.

Peters, J. M., H. Morrison, T. C. Nelson, J. N. Marquis, J. P. Mulholland, and C. J. Nowotarski, 2022c: The influence of shear on deep convection initiation. Part II: Simulations. *J. Atmos. Sci.*, **79**, 1691–1711.

Peters, J. M., J. P. Mulholland, and D. R. Chavas, 2022a: Generalized lapse rate formulas for use in entraining CAPE calculations. *J. Atmos. Sci.*, **79**, 815–836.

Rasmussen, E. N., and D. O. Blanchard, 1998: A baseline climatology of sounding-derived supercell and tornado forecast parameters. *Wea. Forecasting*, **13**, 1148–1164.

Rasmussen, E. N., and J. M. Straka, 1998: Variations in supercell morphology. Part I: Observations of the role of upper-level storm-relative flow. *Mon. Wea. Rev.*, **126**, 2406–2421.

Riehl, H., and J. S. Malkus, 1958: On the heat balance in the equatorial trough zone. *Geophysica*, **6**, 503–538.

Romps, D. M., 2016: The stocastic parcel model: A deterministic parameterization of stochastically entraining convection. *J. Adv. Model. Earth Syst.*, **8**, 319–344.

Rosenfeld, D., and Coauthors, 2008: Flood or drought: How do aerosols affect precipitation? *Science*, 321 (5894), 1309–1313.

Accepted for publication in *Monthly Weather Review*. DOI 10.1175/MWR-D-23-0166.1.

Rotunno, R., and J. B. Klemp, 1985: On the rotation and propagation of simulated supercell thunderstorms. *J. Atmos. Sci.*, **42**, 271–292.

Schenkman, A. D., M. Xue, and D. T. Dawson II, 2016: The cause of internal outflow surges in a high-resolution simulation of the 8 May 2003 Oklahoma City tornadic supercell. *J. Atmos. Sci.*, **73**, 353–370.

Schueth, A., C. Weiss, and J. M. L. Dahl, 2021: Comparing observations and simulations of the streamwise vorticity current and the forward-flank convergence boundary in a supercell storm. *Mon. Wea. Rev.*, **149**, 1651–1671.

Skinner, P. S., C. C. Weiss, M. M. French, H. B. Bluestein, P. M. Markowski, and Y. P. Richardson, 2014: VORTEX2 observations of a low-level mesocyclone with multiple internal rear-flank downdraft momentum surges in the 18 May 2010 Dumas, Texas, supercell. *Mon. Wea. Rev.*, **142**, 2935–2960.

Smith, J. A., M. L. Baeck, Y. Zhang, and C. A. Doswell III, 2001: Extreme rainfall and flooding from supercell thunderstorms. *J. Hydrometeor.*, **2**, 469–489.

Snyder, J. C., H. B. Bluestein, D. T. Dawson, and Y. Jung, 2017: Simulations of polarimetric, X-band radar signatures in supercells. Part II: ZDR columns and rings and KDP columns. *J. Appl. Meteor. Climatol.*, **56**, 2001–2026.

Straka, J. M., E. N. Rasmussen, R. P. Davies-Jones, and P. M. Markowski, 2007: An observational and idealized numerical examination of low-level counter-rotating vortices toward the rear flank of supercells. *Electron. J. Severe Storms Meteor.*, **2**, 1–22.

Tanamachi, R. L., L. J. Wicker, D. C. Dowell, H. B. Bluestein, D. T. Dawson II, and M. Xue, 2013: EnKF assimilation of high-resolution, mobile Doppler radar data of the 4 May 2007 Greensburg, Kansas, supercell into a numerical cloud model. *Mon. Wea. Rev.*, **141**, 625–648.

Accepted for publication in *Monthly Weather Review*. DOI 10.1175/MWR-D-23-0166.1.

Thompson, R. L., R. Edwards, J. A. Hart, K. L. Elmore, and P. Markowski, 2003: Close proximity soundings within supercell environments obtained from the Rapid Update Cycle. *Wea. Forecasting*, **18**, 1243–1261.

Thompson, R. L., R C. M. Mead, and R. Edwards, 2007: Effective storm-relative helicity and bulk shear in supercell thunderstorm environments. *Wea. Forecasting*, **22**, 102–115.

Trapp, R. J., G. R. Marion, and S. W. Nesbitt, 2017: The regulation of tornado intensity by updraft width. *J. Atmos. Sci.*, **74**, 4199–4211.

Trier, S. B., and D. B. Parsons, 1995: Updraft dynamics within a numerically simulated subtropical rainband. *Mon. Wea. Rev.*, **123**, 39–58.

Unidata, 2021: MetPy: A Python Package for Meteorological Data, version 1.1.0. UCAR/Unidata, accessed 1 July 2023.

Warren, R. A., H. Richter, H. A. Ramsay, S. T. Siems, and M. J. Manton, 2017: Impact of variations in upper-level shear on simulated supercells. *Mon. Wea. Rev.*, **145**, 2659–2681.

Weisman, M. L., and J. B. Klemp, 1982: The dependence of numerically simulated convective storms on vertical wind shear and buoyancy. *Mon. Wea. Rev.*, **110**, 504–520.

Weisman, M. L., and J. B. Klemp, 1984: The structure and classification of numerically simulated convective storms in directionally varying wind shears. *Mon. Wea. Rev.*, **112**, 2479–2498.

Weisman, M. L., and R. Rotunno, 2000: The use of vertical wind shear versus helicity in interpreting supercell dynamics. *J. Atmos. Sci.*, **57**, 1452–1472.

Wicker, L. J., and R. B. Wilhelmson, 1995: Simulation and analysis of tornado development and decay within a three-dimensional supercell thunderstorm *J. Atmos Sci.*, **52**, 2675–273.

Accepted for publication in *Monthly Weather Review*. DOI 10.1175/MWR-D-23-0166.1.

Zhang, G. J., and N. A. McFarlane, 1991: Convective stabilization in midlatitudes. *Mon. Wea. Rev.*, **119**, 1915–1928.

Zhang, G. J., 2009: Effects of entrainment on convective available potential energy and closure assumptions in convective parameterization. *J. Geophys. Res.*, **114**, D07109.

File generated with AMS Word template 2.0

Accepted for publication in *Monthly Weather Review*. DOI 10.1175/MWR-D-23-0166.1.